Title

Liposomal Delivery of Mitoxantrone and a Cholesteryl Indoximod Prodrug Provides Effective Chemo-immunotherapy in Multiple Solid Tumors

Journal

ACS Nano, 14(10)

ISSN

1936-0851

Authors

Mei, Kuo-Ching
Liao, Yu-Pei
Jiang, Jinhong
et al.

Publication Date

2020-10-27

DOI

10.1021/acsnano.0c05194

Peer reviewed

HHS Public Access

Author manuscript

ACS Nano. Author manuscript; available in PMC 2021 October 27.

Published in final edited form as:

ACS Nano. 2020 October 27; 14(10): 13343–13366. doi:10.1021/acsnano.0c05194.

Liposomal Delivery of Mitoxantrone and a Cholesteryl Indoximod Prodrug Provides Effective Chemo-Immunotherapy in Multiple Solid Tumors

Kuo-Ching Mei[1,2], **Yu-Pei Liao**[1,2], **Jinhong Jiang**[2], **Michelle Chiang**[2], **Mercedeh Khazaieli**[2], **Xiangsheng Liu**[1,2], **Xiang Wang**[2], **Qi Liu**[2], **Chong Hyun Chang**[2], **Xiao Zhang**[1], **Juan Li**[1], **Ying Ji**[1], **Brenda Melano**[2], **Donatello Telesca**[3], **Tian Xia**[1,2], **Huan Meng**[1,2,4], **Andre E. Nel**[1,2,4]

[1]Division of NanoMedicine, Department of Medicine, David Geffen School of Medicine University of California, Los Angeles, California, 90095, United States

[2]California NanoSystems Institute, University of California, Los Angeles, California 90095, United States

[3]Department of Biostatistics, University of California, Los Angeles, California, 90095, United States

[4]Jonsson Comprehensive Cancer Center, University of California, Los Angeles, California, 90095, United States

Abstract

We developed a custom-designed liposome carrier for co-delivery of a potent immunogenic cell death (ICD) stimulus plus an inhibitor of the indoleamine 2,3-dioxygenase (IDO-1) pathway to establish a chemo-immunotherapy approach for solid tumors in syngeneic mice. The carrier was constructed by remote import of the anthraquinone chemotherapeutic agent, mitoxantrone (MTO), into the liposomes, which were further endowed with a cholesterol-conjugated indoximod (IND) prodrug in the lipid bilayer. For proof-of-principle testing, we used IV injection of the MTO/IND liposome in a CT26 colon cancer model to demonstrate the generation of a robust immune response, characterized by the appearance of ICD markers (CRT and HMGB-1) as well as evidence of cytotoxic cancer cell death, mediated by perforin and granzyme B. Noteworthy, the cytotoxic effects involved natural killer (NK), which suggests a novel type of ICD response. The immunotherapy response was significantly augmented by co-delivery of the IND prodrug, which induced additional CRT expression, reduced number of $Foxp3^+$ Treg and increased perforin release, in addition to extending animal survival beyond the effect of an MTO-only liposome. The outcome reflects the improved pharmacokinetics of MTO delivery to the cancer site by the carrier.

Correspondence should be addressed to: Andre E. Nel, Division of NanoMedicine, Department of Medicine, University of California, Los Angeles, 52-175 CHS, Los Angeles, California 90095, USA. Phone: 310.825.6620; anel@mednet.ucla.edu; Huan Meng, Division of NanoMedicine, Department of Medicine, University of California, Los Angeles, 570 Westwood Plaza, Building 114, Room 6511, Los Angeles, California 90095, USA. Phone: 310.825.0217; hmeng@mednet.ucla.edu.

Competing Financial Interests: Andre E. Nel and Huan Meng are co-founders and equity holders in Westwood Biosciences Inc. and NAMMI Therapeutics. Nel and Meng also serve on the Board for Westwood Biosciences Inc. The remaining authors declare no conflicts of interest.

Supporting Information Available: Additional figures and results, as described in the text. This material is available free of charge *via* the Internet at http://pubs.acs.org

In light of the success in the CT26 model, we also assessed the platform efficacy in further breast cancer (EMT6 and 4T1) and renal cancer (RENCA) models, which overexpress IDO-1. Encapsulated MTO delivery was highly effective for inducing chemo-immunotherapy responses, with NK participation, in all tumor models. Moreover, the growth inhibitory effect of MTO was enhanced by IND co-delivery in EMT6 and 4T1 tumors. All considered, our data support the use of encapsulated MTO delivery for chemo-immunotherapy, with the possibility to boost the immune response by co-delivery of an IDO-1 pathway inhibitor.

Keywords

chemo-immunotherapy; “2-in-1” co-delivery liposome; immunogenic cell death; IDO-1; mitoxantrone; cholesterol prodrug

The repurposing of chemotherapy to induce anti-tumor immune responses, in addition to reliance on cancer-killing properties, introduces a powerful new strategy to control cancer growth and metastases. Several chemotherapeutic drugs have been identified that are capable of inducing immunogenic cell death (ICD) based on DNA damage as the primary injury mechanism, combined with collateral cellular stress that generates immunological danger signals.[1, 2] Briefly, ICD represents a specialized form of tumor cell death in response to treatment with select chemotherapeutic agents (*e.g.,* cyclophosphamide, oxaliplatin, paclitaxel, doxorubicin, epirubicin, idarubicin, mitoxantrone, bleomycin, and bortezomib), radiation therapy, or photodynamic therapy (Figure 1A).[3-6] ICD facilitates the presentation of tumor antigens by dendritic cells (DC) based on calreticulin (CRT) expression on the dying tumor cell surface. CRT provides an “eat-me” signal for DC uptake.[7, 8] In addition, dying tumor cells are capable of generating adjuvant stimuli, including high mobility group box 1 (HMGB-1) protein (a toll-like receptor 4 ligand) and ATP release, which supports DC maturation and antigen presentation to naïve T-cells.[7-12] T-cell activation leads to the recruitment of cytotoxic T cells (CTLs) to the tumor site, where perforin and granzyme B release is capable of inducing cytotoxic cancer cell death.[13-15] In addition to the role of CTLs, some chemo agents (such as mitoxantrone) also generates cell stress in natural killer (NK) cells, which could participate in the immune response, including through the release of perforin and granzyme B.[13-18]

In spite of long-standing awareness of the ICD response, drugs capable of engaging this pathway are approved for chemotherapy, but not for off-label immunotherapy use.[3, 4] While it is possible that treatment success in the clinic may have benefited from the co-incident ICD effects of some of these drugs, the deliberate use of chemo-immunotherapy has not as yet emerged as a treatment option. However, with the advent of immune checkpoint inhibitor (ICI) therapy, now is an opportune moment to reflect on the use of chemo-immunotherapy from the perspective of checkpoint blocking antibodies operating best when CTLs are present in the tumor microenvironment (TME), also referred to as a “hot” TME.[19-21] Thus, ICD offers the opportunity to turn non-inflamed or “cold” tumors “hot”, as suggested by the enhanced response to checkpoint blocking antibodies in patients with breast, ovarian, or colon cancer receiving neoadjuvant therapy with doxorubicin, paclitaxel, or oxaliplatin.[9, 11, 22-26] Moreover, combination therapy makes sense from the perspective that the

generation of a hot TME by ICD is accompanied by IFN-γ production, which is capable of inducing transcriptional activation of the PD-L1 and indoleamine 2,3-dioxygenase (IDO-1) promotors (Figure 1B).[27-30] This amounts to a counter-regulatory response in which the PD-1/PD-L1 axis or the immunometabolic IDO-1 pathway opposes the immunogenic effects of ICD. IDO-1 is the first and rate-limiting enzymatic step in the catabolism of tryptophan in the kynurenine pathway, leading to robust immune suppression as a result of tryptophan (TRP) depletion and kynurenine (KYN) excess (Figure 1C).[31]. To summarize, the immune-metabolic effects of IDO-1 leads to: (i) negative regulation of the mTOR/P-S6 kinase pathway (T-cell activation); (ii) stimulation of the aryl hydrocarbon receptor (AhR) pathway that promotes IDO-1 expression as well as Treg generation; and (iii) activation of a serine/threonine-protein kinase, GCN2 (general control nonderepressible 2) kinase, which increases IL-6 production and Treg development.[29, 31] Moreover, IL-6 also engages in in an auto-feedback loop that promotes further IDO-1 overexpression (Figure 1C).

All considered, the data in Figure 1 highlights the emerging opportunity to use combination immunotherapy, which blends the use of chemo-immunotherapy with immune checkpoint inhibitors or pharmacological inhibitors of IDO-1. However, while we are aware of the favorable response outcomes of combining neoadjuvant therapy with checkpoint blocking antibodies,[32, 33] not all cancers respond equally to the treatment combinations for a variety of reasons, including heterogeneous immune escape mechanisms.[34, 35] Thus, it has also been demonstrated that inhibitors of the IDO-1 pathway can be combined with ICD-inducing chemo to inhibit tumor growth, *e.g.,* the combination of the IDO-1 inhibitor, NLG919, with doxorubicin in a murine breast cancer model (4T1),[36] or combining NLG919 with paclitaxel for a synergistic anti-cancer effect in a B16-F10 melanoma model.[37] In addition to the heterogeneity of the immune landscape among different cancers, combination therapy has to consider differences in the pharmacokinetics (PK) of the drugs and their biodistribution to the tumor site to generate synergistic or additive response outcomes. From this perspective, nanoparticles offer the advantage of improving the PK of chemotherapeutic drugs, as well as their ability to co-deliver synergistic drug combinations or improving drug toxicity.[24, 38-41] These considerations are particularly important to studies where the experimental effects of anthracyclines and mitoxantrone (MTO) could be seen to be improved in melanoma, breast cancer, and colon cancer models by encapsulated drug delivery.[24, 42, 43] Moreover, it has also been demonstrated that encapsulated chemo delivery can be enhanced by co-administration of checkpoint blocking antibodies.[24, 44, 45] A key question, therefore, becomes whether an immune escape pathway inhibitor can be combined with an ICD stimulus in the same nanocarrier?

In this communication, we concentrate on the immunotherapy potential of MTO, a topoisomerase II inhibitor, which is FDA approved for the treatment of acute leukemia, non-Hodgkin's lymphoma, breast, and prostate cancer.[46-48] Not only does our preliminary data indicate that MTO is a more robust ICD inducer than doxorubicin and oxaliplatin, but introduces a drug that is infrequently used for solid tumor chemotherapy and therefore reduces the frequency of drug resistance in cancers that have been prior treated with first-line drugs, which render them less effective.[4, 49] Moreover, in its therapeutic application for progressive multiple sclerosis, MTO has been shown to exert a potent effect on NK cell maturation, which could boost the immunogenic effects at the tumor site.[16] It is possible,

therefore, that MTO may allow us to engage an unusual or no ICD response pathway. In addition to developing an effective remote loading technique for MTO in a liposomal carrier, we asked whether it was possible to endow the liposomes with an IDO-1 inhibitor, indoximod (IND),[29, 50] which could be introduced into the lipid bilayer by synthesizing a lipid-conjugated prodrug. We demonstrate the development of a dual delivery liposome that could be used effectively for chemo-immunotherapy in four different animal tumor models, demonstrating in 3 of these that the ICD-induced effect can be significantly boosted by an IDO-1 pathway inhibitor. We also obtained evidence for the involvement of NK cells in the MTO immune response. These data demonstrate the feasibility of developing synergistic chemo-immunotherapy, premised on the use of a dual delivery liposome.

Results/Discussion

Mitoxantrone (MTO) Generates Potent ICD Effects in Cancer Cells

The ability of MTO to induce ecto-CRT expression on the tumor cell surface, coupled with the release of HMGB1 (TLR4 agonist) from the nucleus, was tested in CT26 colon cancer cells, along with two additional ICD-inducing agents, doxorubicin (DOX) and oxaliplatin (OXA).[9, 11, 51] Following exposure to 1 or 10 μM of each of the chemotherapeutic agents, flow cytometry analysis was used to assess CRT expression on the dying tumor cells, in addition to the use of a commercial ELISA kit to assess HMGB1 release into the culture medium. This demonstrated significantly higher CRT expression and HMGB1 release by 10 μM MTO compared to the same dose of DOX or OXA (Figure 2A-B). This confirms earlier studies showing the robust effect of MTO on ICD responses in various tumor types, including melanoma,[42, 52] breast cancer,[53] and colon cancer.[49]

Development of MTO and Indoximod (IND) Dual Delivery Liposomes

It was previously demonstrated that MTO encapsulation into PEGylated liposomes could enhance the antineoplastic efficacy of the drug due to improved pharmacokinetics (PK) and reduced toxicity.[38, 40, 41, 54, 55] In addition to these therapeutic advantages, we were interested in the ability of the liposomal carrier to provide dual drug delivery, *e.g.,* combining the immunogenic effects of MTO with an inhibitor of the IDO-1 immune metabolic pathway. Figure 1B explains the rationale of the dual delivery platform, aiming to develop a “2-in-1” liposome that co-delivers MTO with a non-competitive inhibitor of the IDO-1 pathway, IND (Figure 3A). Although it is possible to consider passive co-entrapment of the drugs, this only provides a low-loading option, in addition to a ratiometric design challenge. Instead, we custom-designed a dual delivery liposome based on the principles that MTO is a weak base that can be remotely imported into the liposome by a proton gradient, allowing us to use the lipid bilayer to incorporate IND as a cholesterol-conjugated prodrug (Figure 3A, **right panel**).

Guided by medicinal chemistry criteria, we identified drug amine and carboxyl groups as possible IND groups to be considered for conjugation reactions that preserve the drug’s planar structure.[56] After considering several design options, cholesteryl was chosen as the conjugation partner for synthesizing a “Chol-IND” prodrug (Figure 3A). Drug conjugation to cholesterol was carried out in 4 steps (Figure 3B). First, the IND primary amine was

protected by tert-butoxycarbonyl (*tert*-Boc) (step 1), allowing the carboxyl group to be used for Steglich esterification to cholesterol (step 2).[57] The acid-sensitive *tert*-Boc group was subsequently removed by trifluoroacetic acid (TFA), yielding the Chol-IND-NH_3^+ TFA^- salt (step 3). The salt was removed by ion-exchange resin, yielding Chol-IND-NH_2 as a free-base (step 4). High-resolution mass spectroscopy (MS) confirmed the synthesis of Chol-IND (Figure 3C). Further details of the ^1H NMR and MS spectra of the prodrug appears online (Figure S1).

Construction of the MTO/IND liposome (L-MTO/IND) was accomplished by using a traditional lipid film (LF) hydration method, as outlined in Figure 4A. Briefly, the lipid blend (< 30 mg total lipid), including Chol-IND, was dissolved in an organic solvent (step 1), followed by solvent evaporation (rotary evaporator) to form a lipid film in a round bottom flask (step 2). To accomplish MTO encapsulation, we used a previously validated method for remote MTO import that utilizes citrate as a trapping agent.[39] In brief, the lipid film was hydrated in a citrate acid-sodium citrate buffer (pH 4), followed by vortexing to obtain multi-lamellar liposomal dispersion (step 3). Stepwise extrusion through polycarbonate membranes was used to obtain 100-120 nm uni/dual-lamellar liposomes (step 4a), from which free citrate was removed by buffer exchange (step 4b). Liposomes loaded with the trapping agent were incubated in water-soluble MTO·2HCl at pH 7.4 for 1 h at 65 °C, allowing MTO·2HCl to diffuse across the lipid bilayer. This leads to drug protonation and precipitation in the acidic liposomal interior (step 5). The non-encapsulated MTO was removed by size-exclusion chromatography to yield purified MTO/IND-liposomes (step 6). An important control was the synthesis of a liposome incorporating MTO only (L-MTO) (*i.e.,* no prodrug incorporation), as well as a liposome that contains IND only (L-IND), with no MTO loading.

An important caveat for embedding Chol-IND into a lipid bilayer with the composition DSPC: Chol-IND: DSPE-PEG_{2kDa} = 55: 40: 5 (m/m) was to take into account the ionization potential of the prodrug, including the impact that this could have on the ζ-potential. The presence of an ionizable amine on the prodrug (Chol-IND-NH_3^+) was responsible for the formation of a cationic liposome at pH 7.4 (Formulation 1, Figure S2). Since a nanocarrier with a cationic charge could be rapidly cleared from the circulation, our aim was to produce a liposome with a modestly negative ζ-potential.[30] Fine-tuning of the ζ-potential was achieved by introducing cholesteryl hemisuccinate (CHEMS), which contains an ionizable carboxyl group (pKa ≈ 5.8), capable of neutralizing the cationic charge of the prodrug. Making use of an iterative approach to achieve a negatively charged liposome, we determined that at a molar ratio 45: 30: 20: 5 for DSPC, Chol-IND, CHEMS, and DSPE-PEG_{2kDa} we could construct an L-MTO/IND liposome with ζ-potential −11.6 mV in pH 7.4 PBS (Formulation 4, Figure S2). The Chol-IND content of this formulation was 30% m/m for the lipid bilayer, which is equivalent to a 22.9% w/w ratio of the prodrug/total lipid content (8.5% w/w IND/total lipid). In order to assess the impact of charge neutralization, ζ-potential analysis was performed at pH values ranging from 3.8 to 7.4 (Figure 4B). This demonstrated that while the L-MTO/IND liposomes exhibited a cationic charge at pH ≤ 6.4, the ζ-potential shifted to negative values above pH 6.4. The charge neutralization differed from the behavior of a control liposome that was constructed to deliver MTO only (L-MTO) by replacing Chol-IND with unconjugated cholesterol, while maintaining the presence of

CHEMS. L-MTO displayed a ζ-potential of −45 mV at pH 7.4 (PBS), which remained in the negative range, even with a pH drop to 3.8 (−20 mV) (Figure 4B). The charge reversal of L-MTO/IND could be of importance in the biodistribution of this liposome, as will be discussed later.

The L-MTO and the L-MTO/IND liposomes were also comprehensively characterized for morphology, size, size distribution and stability. CryoEM micrographs showed that both formulations yielded uniform spherical structures, containing a drug precipitate in the cores (Figure 4C). Dynamic light scattering demonstrated hydrodynamic sizes of 112 ± 2 nm and 98 ± 1 nm for L-MTO and L-MTO/IND, respectively, with corresponding PDIs of 0.017 and 0.014 (Figure 4C). In order to assess the stability of the carrier, L-MTO/IND liposomes were stored in PBS (pH 7.4) for three months at 4°C. Assessment of the hydrodynamic size (93.5 ± 1.3 nm), PDI index (0.089), ζ-potential (−9.16 ± 0.9 mV), and morphology did not show any significant change over 3 months in storage (Figure S3). Moreover, MTO and IND leakage or release remained below 1% of the starting dose; this confirms the stability of the liposomes in storage (Figure S3).

In order to assess the drug release characteristics of the prodrug *in Vitro*, a liposome was constructed to include IND only (L-IND). This carrier was introduced into a culture of CT26 colon cancer cells to assess the effect on phosphorylation of S6 kinase (S6K), which is activated downstream of mTOR, a target of IDO-1 inhibition.[58] CT26 cells were pre-treated with IFN-γ overnight to stimulate IDO-1 expression. The results were compared to treatment with equal amounts of free IND, introduced at 1, 10, and 50 μM in a tryptophan deficient medium for 6 h. Use of an immunoblotting approach to assess the ratio of phosphorylated S6 kinase (P-S6K) *vs.* total S6K ratios,[58] demonstrated that the ratios of 1.8, 4.2 and 7.5 at free IND concentrations 1, 10, and 50 μM, increased to 5.0, 8.0 and 10.4, respectively, during encapsulated delivery of the prodrug (Figure S4). MTO release will be discussed below.

The Pharmacokinetics (PK) of MTO Delivery in the CT26 Colon Cancer Model

The PK of MTO delivery by liposomes was compared to free drug treatment in CT26 colon cancer-bearing mice. The MTO dose was chosen based on calculations of the maximum tolerated dose (MTD) in Balb/c mice (Figure S5). This yielded dose calculations of ~4 mg/kg and ~30 mg/kg for free and encapsulated MTO, respectively, leading to the decision to use a liposomal dose of 3 mg/kg intravenously (IV), followed by blood collection after 5 min, 15 min, 30 min, 1 h, 2 h, 4 h, 24 h, and 24 h (n = 3 per time point). Tumors were harvested at 24 h and 48 h (n = 3). The methodology for HPLC analysis appears online (Figure S6). While free MTO rapidly disappeared from the blood (< 60 min), treatment with both liposomes showed a significant prolongation of the serum drug concentration (Figure 5A), allowing us to calculate the parameters for area under the curve (AUC), distribution half-life ($T_{1/2}\alpha$) and elimination half-life ($T_{1/2}\beta$) as shown in Figure 5B. Interestingly, these results showed a significant difference between the half-life of the liposomes during the elimination phase, with L-MTO/IND exhibiting a $T_{1/2}\beta$ of 10.4 h compared to 15.3 h for L-MTO. This difference is likely due to the increased rate of clearance of the dual delivery liposome, based on charge reversal (as will be discussed later).

In terms of intratumor drug concentrations, both liposomes yielded a much higher MTO concentration than the free drug at 24 and 48 h ($p<0.001$) (Figure 5C). Moreover, it is also of interest that the intratumor MTO content declined more rapidly for L-MTO than for L-MTO/IND over 48 h (Figure 5C). We ascribed this to differences in carrier stability, as demonstrated by studying MTO release from the carriers during abiotic exposure to 50% fetal bovine serum (FBS), with the assistance of IVIS imaging (Figure S7). IVIS imaging makes use of the properties of MTO as a fluorescent molecule, which can be viewed at $\lambda_{ex/em}$ of 675/703 nm (Cy5.5 channel).[59] When contained in its liposome-encapsulated, precipitated state, MTO fluorescence was quenched, but reappeared upon drug release from the liposome (Figure S7A). The stability differences between the liposomes is demonstrated by the increased fluorescence intensity of the L-MTO compared to the L-MTO/IND carrier in the presence of PBS or FBS for 48 h (Figure S7B and S7C).

The MTO fluorophore properties allowed us to quantitatively assess MTO biodistribution to the CT26 colon tumor site, following intravenous (IV) injection of a 3 mg/kg dose of the free *vs.* the encapsulated MTO. Following animal sacrifice, major organs were collected 24 h or 48 h post IV injection for IVIS imaging and assessment of fluorescence intensity through the use of Living Image® software v4.5 (PerkinElmer). Representative *ex-vivo* IVIS images of harvested tumors and organs are shown in Figure S8A, which demonstrates MTO release at the tumor sites from the biodistributed carriers. Fluorescence intensity, expressed as normalized radiant efficiency ([p/s/cm^2/sr]/[μW/cm^2]) at 24 h or 48 h, is shown in Figures S8B and S8C, respectively. Both liposomes accomplished a 9-10-fold increase in MTO fluorescence intensity at the tumor site compared to the free drug, without significant differences. There was also a significant increase in drug uptake in the liver and spleen during liposomal delivery, while biodistribution to the lung was decreased.

Dual Drug Delivery Induces an Effective ICD-Induced Immunotherapy Response in the CT26 Colon Cancer Model

The CT26 syngeneic mouse model is frequently used to assess the therapeutic efficacy of ICI antibodies.[60] We asked whether the liposomal MTO delivery can generate immunogenic effects in this tumor model and whether the response can be augmented by interfering in the IDO-1 pathway. The experimental design of the efficacy study is shown in Figure 6A, which demonstrates the animals receiving 4 injections of the encapsulated MTO, every 3 days. Treatment commenced when subcutaneous tumor sizes approached 100-150 mm^3. Based on the MTD calculations (Figure S5), we decided on a liposome MTO dose of 3 mg/kg for each injection. This provided a cumulative dose of 12 mg/kg MTO after 4 injections. Due to lethal toxicity at a cumulative dose >4mg/kg, it was not possible to use free MTO in the study (Figure S5A). The corresponding Chol-IND dose was 2.8 mg/kg IND per injection (11.2 mg/kg cumulative drug dose). The therapeutic effect of L-MTO/IND was compared to saline, empty liposomes (L), an MTO only liposomes (L-MTO; cumulative drug dose 12 mg/kg), and an IND-only liposome (L-IND; cumulative drug dose11.2 mg/kg). The tumor growth curves ($n = 7$), reflecting mean tumor sizes in live animals at different time points, appear in the left-hand panel of Figure 6A, while the individual growth curves for each animal are shown in the spaghetti plots in Figure S9. The size measurements were accompanied by the appearance of a blue/green tumor discoloration, which reflects the

presence of the delivered MTO (Figure 6A, lower-right panel). Both L-MTO and L-MTO/IND liposomes were effective in suppressing tumor growth, leading to statistically significant decreases in tumor size, which was not seen with empty liposomes (L) or L-IND (left-hand panel).

Although we did not observe a significant difference in tumor shrinkage for liposomes that incorporated or excluded Chol-IND, significant differences resulted from the inclusion of IND during immunohistochemistry (IHC) analysis for ICD markers (Figures 6B-6E and Figure 7). The first analysis was to assess the expression of the ICD markers (CRT, HMGB1, and LC3B)[9] in the TME, as explained in Figure 1A. LC3B is a biomarker for autophagy,[61] as an integral component of the ICD response at the tumor site.[62] Not only did we observe that CRT staining intensity was increased significantly by L-MTO as well as L-MTO/IND ($p < 0.0001$), but also that the staining intensity was significantly higher ($p < 0.0001$) for L-MTO/IND (5-fold) compared to L-MTO (2.7-fold) (Figure 6B), presumably due to higher MTO retention at the tumor site (Figure 5E).These findings were also reflected during the visual inspection of the IHC slides (right side panel). The same trends were observed in evaluating HMGB1 and LC3B staining intensities, which were significantly increased for L-MTO and L-MTO/IND, without differentiating between these treatments (Figures 6C-D, Figure S10-S11).

Additional IHC analysis was carried out to assess IDO-1 expression, which demonstrated that while encapsulated MTO induced a significant increase in enzyme expression when compared to the untreated control ($p < 0.0001$), co-delivery of IND could significantly decrease (36%) the staining intensity when compared to L-MTO (Figure 6E).[29, 31] This could reflect the role of the IDO-1 inhibitor in disrupting IDO-1 expression as a result of the AhR/IL-6-catalyzed auto-feedback loop (Figure 1C).[63] These results are confirmed by representative IHC images, shown in the right-hand panel. An apparent slight reduction in IDO-1 staining intensity during L-IND treatment was not statistically significant.

In light of the immunogenic effects of MTO, we also investigated cognate immune responses in the CT26 animal model. This included assessment of cytotoxic T-cell and NK responses, both of which are impacted by MTO.[15, 18, 28, 64, 65] First, we assessed IFN-γ production as a biomarker that reflects recruitment of CTLs or NK cells to the tumor site (Figure 1B). Both liposomal carriers were associated with IFN-γ expression, as determined by visual inspection of staining intensity as well as computational analysis of the pixel density ($p < 0.0001$) (Figure 7A). The second IHC analysis was for perforin expression, showing a significant effect for L-MTO, which was further enhanced by IND co-delivery ($p < 0.001$) (Figure 7B). The same was true for granzyme B staining intensity (Figure S12). An interesting finding for CTL IHC analysis was a significant decrease in the number of $CD8^+$ T-cells per mm^2 during treatment with the MTO-encapsulating liposomes, compared to a significant 1.8x increase in $CD8^+$ density in response to L-IND. There was also a slight but statistically significant 1.7x increase in $CD8^+$ density for the dual-delivery liposome compared to L-MTO. The co-delivery of L-IND with MTO was able to mitigate CD8 reduction caused by MTO even when CD8 is significantly suppressed (Figure 7C).[66] In order to explain the increased staining intensity of perforin or granzyme B, IHC analysis was undertaken to look for the presence of p46, a NK cell-specific surface molecule that

mediates cell activation.[67] NK cell participation in anti-tumor immune responses have been demonstrated in response to treatment with bortezomib, doxorubicin, and cyclophosphamide.[17, 68] Moreover, MTO promotes NK maturation in multiple sclerosis patients.[16] Noteworthy, we demonstrated a 6-fold increase in NKp46$^+$ cell number during treatment with L-MTO and L-MTO/IND, both resulting in a statistically significant increase ($p < 0.001$) of this biomarker (Figure 7D). Utilizing the Opal Multiplex IHC platform from Akoya Biosciences for multi-color staining of tumor slices from untreated *vs.* L-MTO/IND treated animals, we confirmed that the triple color staining with DAPI (blue nuclei), perforin (green) and NKp46$^+$ (red) could demonstrate that the perforin staining occasionally overlaps with the localization of NK cells, resulting in composite yellow-brown stained cells (Figure 7E). In contrast, triple color staining for DAPI (blue), perforin (green), and CD8$^+$ (magenta) cells demonstrated a decrease or disappearance of CD8$^+$T-cells in tumor sections from MTO/IND treated animals (Figure 7E). These results strongly suggest that the newly recruited NK cells are indeed responsible for perforin deposition, which could be observed despite the absence of T-cells from the tumor site.

The cytolytic action of NK cells (and CTLs) can be opposed by the recruitment of Foxp3$^+$ regulatory T cells (Treg) to the tumor site. Moreover, Treg frequency is increased by IDO-1 action and decreased by interference in this pathway.[69] IHC staining for the presence of Foxp3$^+$ cells demonstrated a significant reduction in staining intensity for this biomarker in animals treated with L-IND alone, as well as treatment with both MTO-delivering liposomes (Figure S13A). Noteworthy, the decline in Treg density was most pronounced (95% decline) for treatment with L-MTO/IND, which was significantly lower ($p < 0.01$) than the already significant response to L-MTO (Figure S13A). Moreover, when used in conjunction with the NKp46 data, the calculation of NKp46/Treg ratios showed an increase from a ratio of 0.15 in the untreated control to 4.2 (28-fold) and 22 (150-fold), respectively, for L-MTO and L-MTO/IND (Figure S13B). It was also possible to calculate the CD8/Treg ratios for each group, allowing us to demonstrate that the highest value could be achieved in the L-MTO/IND group (Figure S13C).

Kaplan-Meier Analysis to Demonstrate The Survival Effect of Encapsulated Dual Drug Delivery in The CT26 Colon Cancer Model

Since our efficacy analysis (Figures 6-7) showed that the MTO immune response could be augmented by IND, we asked whether dual drug delivery could impact animal survival beyond the 23-day observation period in the efficacy study. The experimental procedure was identical to the efficacy study, except that after the 4th treatment, the animals were observed until death or approaching moribund criteria that warrant animal sacrifice. The survival data were plotted as Kaplan-Meier graphs that were further analyzed by the Log-rank/Mantel-Cox test (Figure 8A). This demonstrated that treatment with the L-MTO/IND liposome showed a statistically significant increase ($p < 0.001$) in animal survival compared to the L-MTO liposome. One animal in the dual-delivery group survived tumor-free. Plotting of tumor sizes in the same experiment, demonstrated that both L-MTO and L-MTO/IND could significantly interfere in tumor growth by day 23 ($p < 0.01$), but without a significant difference in tumor size (Figure 8B). However, beyond day 23, L-MTO/IND was significantly more effective than L-MTO at several time points, *e.g.,* day 24 ($p < 0.05$), day

26 ($p < 0.01$) and day 38 ($p < 0.01$) (Figure 8B). The corresponding spaghetti tumor growth curves confirm the enhanced effect in the dual-delivery group (Figure 8C). These data would seem to imply that the augmentation of the immune response by IND made a significant difference beyond day 23, likely as a result of augmentation of the immune response that was initiated by MTO.

The Efficacy of The Dual-Delivery MTO/IND Liposome Also Applies to Other Syngeneic Cancer Models

From the perspective of heterogeneous immune landscapes determining the success of the ICD-induced immune response, our data in the CT26 cancer model demonstrate that interference in the IDO-1 pathway can effectively enhance MTO immunogenic effects. Since IFN-γ production by the ICD response may help to explain this finding (Figure 1B), we asked whether additional syngeneic models could be used to evaluate the role of IND in TMEs where IFN-γ leads to IDO-1 expression. We demonstrated, through the use of an immunoblotting approach, a 5-fold increase in IDO-1 expression in CT26 cells (Figure 9A). After surveying a range of available cancer cell lines from Charles River Labs that can be used to assess therapeutic efficacy in syngeneic tumor immune models, we identified three additional cell lines that showed increased IDO-1 expression in response to IFN-γ exposure (Figure 9A). These included: (i) the EMT6 breast cancer cell line, ranked as moderately responsive to ICIs; (ii) the RENCA renal cancer cell line, characterized as moderately responsive to ICIs, and (iii) the 4T1 triple-negative breast cancer line, regarded as resistant to ICIs.[70, 71] Western blotting demonstrated a 29, 15, and a 15-fold increase in IDO-1 expression in response to IFN-γ in EMT6, RENCA, and 4T1, respectively (Figure 9A). We then asked whether the cellular responses are reflected in the basal IDO-1 expression levels in the corresponding syngeneic tumors by undertaking IHC analysis after tumor harvesting (Figure 9B). This demonstrated a significant increase in the level of IDO-1 expression in EMT6, RENCA, and 4T1 compared to CT26 (upper panel). Interestingly, these tumors also showed increased PD-L1 staining compared to CT26, with 4T1 and RENCA >EMT6 > CT26 (lower panel). Thus, in combination with available data from Charles River on levels of cellular PD-L1 expression and ICI responsiveness of the tumors, we outlined a provisional response projection to conduct studies on the effect of encapsulated MTO, with or without IND co-delivery (Figure 9C).

Before tumor growth could be compared in the syngeneic models, it was necessary to increase liposomal batch sizes (~150 mg) to perform these studies with a single batch of liposomes that can be used for parallel tumor model studies. The bigger batch size required adaptation of the evaporation procedure (step 2) in Figure 4A to ensure homogeneous mixing of the higher lipid amounts used for the synthesis process. This was accomplished by a reverse-phase (RP) method, as detailed in the method section and explained in Figure S14A.[72, 73] Physicochemical characterizations of the newly synthesized carriers showed that the size, zeta potential, and drug loading capacity of the liposomes were comparable to the carrier characteristics obtained in the lipid film hydration method (Figure S14B).

Following the establishment of subcutaneous growing tumors in the animal flanks, IV treatment proceeded to deliver liposomal MTO and IND concentrations of 3 mg/kg and 2.8

mg/kg, respectively, when tumor sizes approached 100-150 mm^3 (Figure 10). Injections were repeated every 3 days for a total of 4 administrations. The respective tumor growth curves (mean ± S.D.), together with tumor images obtained at postmortem harvesting on day 23, are shown Figure 10A (EMT6; $n = 10$), Figure 10B (RENCA; $n = 6$-8), and Figure 10C (4T1; $n = 9$). Successful MTO delivery was reflected by the bluish discoloration of the responding tumors, similar to CT26 (Figure 6A, lower-right panel). The tumors in animals receiving treatment with MTO liposomes also appear less vascular in Figures 10A-10C, which is in agreement with the anti-angiogenic properties of the free drug.[74-76] Noteworthy, in the highly IDO-1 inducible EMT6 breast cancer model, the treatment response to L-MTO/IND was significantly more effective than L-MTO ($p = 0.011$) (Figure 10A). In contrast, in the RENCA model, the efficacy of L-MTO alone sufficed for significant tumor growth inhibition that could not be further improved by IND co-delivery (Figure 10B). However, in the 4T1 breast cancer model, L-MTO/IND administration was significantly ($p < 0.01$) more effective than L-MTO, in spite of the tumor being characterized as immunotherapy resistant (Figure 10C). Spaghetti growth curves and corresponding tumor weights are shown in Figure S15 online. IHC analysis in these experiments to assess CRT, perforin, and NKp46 expression, showed that for each tumor type, it was possible to observe evidence of cytotoxic killing that was accompanied by increased recruitment of NK cells (Figures 10A-10C). Representative IHC images are shown in Figure S16 A-C.

We also utilized the mammary pad implementation of 4T1 cells in Balb/c mice to perform orthotopic tumor studies. First, we performed an efficacy study where tumor growth was followed until animal sacrifice on day 23. This demonstrated that MTO-delivering liposomes were quite effective in reducing tumor growth without a significant difference between L-MTO and L-MTO/IND (Figure S17). However, L-MTO/IND treatment was responsible for considerably higher CRT and HMGB1 expression than L-MTO (Figure S18A), which we ascribed to the increased stability of the dual delivery liposomes as shown in Fig. S7B. Both liposomes significantly increased perforin and granzyme B staining at the tumor site (Figure S18B), while decreasing the number of $CD8^+$ cells, similar to what is seen in CT26 tumors (Figure S18C). Next, we performed a survival study in which Kaplan-Meier analysis showed a significant extension in animal survival in response to both liposomes (Figure S19). While a few of the animals responding to the L-MTO/IND administration survived longer than the L-MTO treatment group, the results were not statistically significant.

Conclusions

In this study, we demonstrate the development of a dual-delivery liposomal carrier for successful chemo-immunotherapy in the colon, breast, and renal cancer through the delivery of an ICD stimulus, coupled with interference in the immune metabolic effects of the IDO-1 pathway. The carrier was constructed by the remote import of the anthraquinone chemotherapeutic agent, MTO, plus incorporation of a cholesterol-conjugated IND prodrug into the lipid bilayer. First, we demonstrated in a CT26 colon cancer efficacy model that IV injection of the MTO/IND carrier could induce a robust immune response that was characterized by the appearance of ICD markers (CRT expression and HMGB-1 release) in the tumor microenvironment, coupled with cytotoxic cancer cell death by the release of perforin and granzyme B from participating NK cells. The immunotherapy response was

significantly augmented by co-delivery of the IND prodrug, which boosted CRT expression and perforin release at the tumor site, in addition to prolonging animal survival beyond the already-significant survival effect of the L-MTO liposome in a follow-up experiment. The therapeutic efficacy of the liposomal carriers was reflected by the enhanced intratumoral MTO content (HPLC) and MTO fluorescence intensity (IVIS) at the cancer site. In light of the proof-of-principle demonstration in the CT26 model, we also assessed the impact of MTO chemo-immunotherapy in two additional breast cancer (EMT6 and 4T1) and renal cancer (RENCA) animal models. These animals also demonstrated a highly significant tumor size reduction in response to treatment by both liposomes, in addition to a significant increase in CRT, perforin, and NKp46 staining (Figure 7, Figure S13). Moreover, the growth inhibitory effect of MTO was enhanced by IND co-delivery in the EMT6 and 4T1 models. All considered, we provide strong evidence to support for the feasibility of using custom-designed liposomal carriers to deliver synergistic drug combinations capable of creating a "hot" TME through an ICD effect, which could be further augmented by combined delivery that intervenes in immune escape mechanisms, *e.g.,* the IDO-1 pathway.

A popular trend in clinical oncology is the successful implementation of neoadjuvant therapy of solid tumors with specific chemo agents such as anthracyclines, platinum drugs, and paclitaxel.[77] The possible explanations for the beneficial effects of the neoadjuvant approach include considerations such as improved tolerance, dose intensity, eradication of occult micro-metastasis, and triggering of anti-tumor immunity.[78] Figure 1 introduces the possibility that the immunogenic effects of a less frequently employed cancer drug, MTO, can be therapeutically exploited, in addition to relying on its chemo effects. Unlike the ICIs that rely on immune priming to initiate immunotherapy, the utility of ICD includes switching "cold" tumors to "hot" through the impact on CRT expression, HMGB1 release, and the initiation of autophagy. It is also important to understand that a lone-standing ICD response could be counter-regulated by upregulated IDO-1 and PD-L1 expression, *e.g.,* as a result of IFN-γ production by the ICD response (Figure 1B). These immune suppressive mechanisms can induce exhaustion of cytotoxic cells as well as Treg recruitment, further silencing the immune response.[29, 31] It is appropriate, therefore, to consider combining ICD immunotherapy with checkpoint inhibitors, exemplified by the use of OXA plus anti-PD-1 in colon cancer,[79] OXA plus anti-PD-L1 in metastatic urothelial cancer,[80], or paclitaxel plus an IDO-1 inhibitor in melanoma.[37] Moreover, we show that the impact on ICD can be further advanced by the improved PK of drug delivery by a liposome, which also allows regional co-delivery of an IDO-1 inhibitor. It is also possible to envisage that a nano-enabled approach could benefit combination treatment strategies that target a host of immune escape pathways. The ability to adjust liposomal composition for co-delivery of multiple treatment combinations may allow us to develop a pipeline of custom-designed carriers to deliver combinations of multiple ICD stimuli,[4] IDO inhibitors,[81] small molecule inhibitors of the PD-1/PD-L1 axis[82-85] and immune adjuvants (*e.g.,* TLR agonists[86, 87]).

MTO was initially approved as a chemotherapeutic agent in 1987 for the treatment of acute leukemia, later receiving additional approval for prostate cancer,[88] metastatic breast cancer, [89] and non-Hodgkin lymphoma.[90] While the mechanism of MTO action can be historically interpreted as to its DNA intercalating or nuclear damaging effects,[91-93] Kroemer *et al.* discovered, during the screening of ~900 anti-cancer compounds, that MTO functions as a

robust ICD inducer.[4] This effect was confirmed in vaccination studies in animals, where MTO resulted in 60% of mice in a fibrosarcoma model being rendered tumor-free.[4] In addition, it was also confirmed that MTO was capable of generating a potent anti-tumor immune response in a CT26 colon cancer model.[62] Other than its use in cancer, MTO has been employed as an immunomodulatory agent for the treatment of multiple sclerosis (MS), [94] where it was demonstrated that its immune-modulatory effects include the expression of $CD8^{low}$ T-cells as well as the enrichment and maturation of NK cells.[16] It is, therefore, of interest that in the generation of ICD at the tumor site, immune perturbation leads to the generation of an anti-tumor immune response that involves $NKp46^{+}$ cells (Figure 7D). Unfortunately, it was not possible to perform IHC staining for cells with a $CD8^{low}$ status. Instead, we observed a decreased number of $CD8^{high}$ T-cells. While NK participation during cancer treatment with MTO is not reported in the literature, there is ample evidence for a number of chemotherapeutic agents that it is possible to observe dose-dependent augmentation of NK cellular effects.[17] Examples include: (i) transcriptional and post-transcriptional regulation of NKG2D by the microtubule inhibitor, vincristine,[95] and (ii) enhanced expression of NKG2D and NKp30 ligands by docetaxel (also a potent inducer of ER stress).[95, 96] From an ICD perspective, it is also interesting that HMGB1 release has been linked to NK maturation, and enhanced crosstalk of these cells with DC.[17] Ecto-CRT expression was also reported to enhance NK-mediated killing in leukemia patients.[97, 98] Another overlap between NK cells and CTL-mediated tumor cell killing, is the production of perforin, granzyme B and IFN-γ by NK cells, as shown in Figure 7.[17] All considered, we propose that consideration be given for repurposing the use of MTO as a chemo agent for wider spread use as a chemo-immunotherapy drug. None of the attempts of using liposomal delivery of MTO in phase I (*e.g.,* NCT02043756, NCT02131688) or phase II (NCT03776279, NCT02596373) clinical trials are currently intended to address a chemo-immunotherapy objective, including for combinatorial use with checkpoint blocking antibodies.

Although several studies have been conducted to look at the ICD-inducing effects of the more frequently used anthracycline agent, doxorubicin, for combination therapy with IDO-1 or checkpoint inhibitors,[36, 45, 99, 100], we prefer the use of MTO for chemo-immunotherapy. The primary reason is the frequent development of drug resistance to doxorubicin in patients who could potentially benefit from chemo-immunotherapy. MTO is used less often, making it more practical to reserve it for use as a chemo-immunotherapy agent that is less likely to encounter drug resistance. Another reason that we resorted to MTO is that it proved difficult to synthesize a liposome with a stable lipid bilayer, capable of supporting a doxorubicin drug precipitate in the presence of a lipid-conjugated prodrug.

Indoximod (IND, 1-methyl-D-tryptophan) is an indirect IDO-1 pathway inhibitor, which is capable of overcoming tryptophan depletion by acting as a tryptophan mimetic (Figure 1C). [50, 101, 102] Currently, there are multiple clinical trials in which IND is combined with chemotherapeutic agents, including ICD inducing drugs. Examples include the combination of IND with (i) cytarabine or idarubicin for acute myeloid leukemia (NCT02835729); (ii) gemcitabine or nab-paclitaxel for pancreatic cancer (NCT02077881); or (iii) docetaxel for solid tumor applications (NCT01191216). There are some limitations, however, in the use of IDO-1 inhibitors as a result of low drug solubility and poor bioavailability. For instance, the

daily dosing requirements for IND is ~400 mg/kg for animal studies[103] and use 1.2~2.4 gram doses in humans[104]. This has prompted pharmaceutical modifications to improve the PK and bioavailability of IND, including synthesis of a leucine-modified hydrochloride salt in the IND prodrug, NLG802, which exhibits a 5-fold improvement in bioavailability.[105] NLG802 has been used for efficacious drug delivery in a B16F10 melanoma model at an IND dose equivalent of 62 mg/kg twice a day.[105] Unlike the salt-based prodrug, the Chol-IND prodrug allows encapsulated delivery by a liposomal bilayer, with the additional advantage of MTO co-delivery. The downstream effects of the Chol-IND prodrug were experimentally proven by observing a reversal of MTO-induced IDO-1 overexpression (Figure 6E), significantly reducing Treg numbers (Figure S13A), and increasing CD8 T-cell expression by L-IND (Figure 7C) at the CT26 tumor site. When combined with MTO, which increases NK cells, the net outcome of the dual delivery liposome is to accomplish the highest NKp46+/Treg values at the tumor site (Figure S13B). All considered, these Chol-IND effects are in good agreement with recently published data from NewLink Genetics,[66] which demonstrated that the major impact of free IND monotherapy in human cancer includes reduced IDO-1 expression, increased CD8 T-cell numbers and reduced Tregs (leading to an increase in CD8/Treg ratios). Through its effect on NK and Tregs, L-MTO/IND liposome outperformed the L-MTO liposome in impacting each of the aforementioned biomarkers. Based on our results with IND, we envisage the versatile use of medicinal chemistry approaches for the dynamic design of liposomes that can be constructed by the development of prodrugs that include IDO-1 inhibitors, small molecule inhibitors of the PD-1/PD-L1 axis, TLR agonists, or NK modulators, etc.

It is also worth commenting on the unique design of our dual delivery liposome through the inclusion of CHEMS to provide charge neutralization IND-Chol-NH_3^+ (Figure S2). This generated a pH-dependent, charge reversible liposome that is negatively charged at physiological pH of 7.4 (*e.g.,* when circulating in the blood), with the possibility of becoming cationic when entering the tumor blood circulation or the TME, where the Warburg effect could lead to dropping the pH to values as low as ~5.5 (Figure 4C). This could be advantageous for nanoparticle uptake and retention at tumor site, in comparison to L-MTO that remains negatively charged (Figure 5C). In addition, the presence of the prodrug also contributes to generating a liposome that is less leaky (Fig. S7B) and maintains intratumor drug concentrations for a longer duration (Fig. 5C).

It is interesting that although the dual delivery liposome was effective for treating 4 different cancer types in representative animal models (Figures 9 and 10), an additive IND effect could only be demonstrated in 2 efficacy studies that were terminated on day 23. From this perspective, it is noteworthy that even though CT26 is regarded as more responsive to immunotherapy, 4T1 is considered treatment-resistant, with EMT6 and RENCA ranking in between.[71, 106] This is in keeping with growing awareness of the heterogeneity of the immune landscape in different cancers and cancer subsets, including cancers depicted as immunologically depleted or presenting an “immune desert”.[107, 108] An additional source of heterogeneity is the expression of one or more immune escape pathways, which include pathways that are regulated by mechanisms different from immune checkpoint receptors.[70, 109-112] Given this background, the successful intervention of our MTO liposomes in all the animal models tested, plus the evidence that the response could be augmented in 3 of the

4 cancer types by co-delivery of IND, is quite impressive. Moreover, for the one tumor that was nonresponsive to IND co-delivery (*i.e.,* RENCA), further survival studies are contemplated to investigate an IND effect on long-term survival outcome, as demonstrated for CT26, which did not show an effect in the first 23 days (Figure 8). All considered this provides a strong incentive to consider the development of the dual-nanocarrier delivery technology for combination immunotherapy in the clinic.

Finally, we want to comment on the limitations of this study. In order to establish proof-of-principle for the combined use of MTO and IND delivery, we designed a liposome for delivery fixed drug ratios, without performing extensive dose-response analysis. It is quite likely that the carrier design can be further improved by dose-finding and synergistic design studies to establish optimal drug ratios, as well as improving the dosing schedule to determine the optimal number of treatments. The dosing interval is of importance to prevent drug side effects such as the palmar-plantar erythrodysesthesia syndrome that is seen with the anthracycline agent, doxorubicin.[113] Since L-IND is pharmacologically active *per se*, it could be interesting to test the combined use of L-IND with other therapeutic approaches, such as CAR-T/NK therapeutics, checkpoint inhibiting antibodies (*e.g.,* anti-PD1/PD-L1, anti-CTLA4), or other nano-formulations (*e.g.,* Doxil®, Onivyde®, Abraxane®). It is also possible to consider additional conjugation techniques for IND to adjust the formulation of the liposomes, including for the purposes of optimizing intratumor drug release and for the upscale production of the liposomes. This could also include design features that maximize stromal vascular access at the tumor site.

In summary, an MTO/IND co-delivery liposome was effective at inhibiting tumor growth in syngeneic mouse cancer models through concurrent induction of ICD and pharmacological inhibition of the IDO-1 pathway at the tumor site. This study provides important pre-clinical data that could serve as the basis of moving this technology forward for effective chemo-immunotherapy of solid tumors in the clinic.

Methods/Experimental

Cell Culture:

The CT26.WT colon cancer cells (CRL-2638™), EMT6 breast cancer cells (CRL-2755™), RENCA renal cancer cells (CRL-2947™), and 4T1 breast cancer cells (CRL-2539™) were obtained from ATCC. The CT26 and 4T1 cells were cultured in RPMI-1640 (ATCC® 30-2001™), supplemented with 10% v/v fetal bovine serum ((#100-106, GeminiBio), penicillin-streptomycin (100 U/mL-100 μg/mL, #15140163, Gibico™), and 2 mM L-alanyl-L-glutamine (#25-015-CI, Glutagro™ Corning®). EMT6 cells were cultured in 85% v/v Waymouth's MB 752/1 medium with 2 mM glutamine (#11220035, Gibico™) and 15% v/v FBS, supplemented with penicillin-streptomycin. RENCA cells were cultured in RPMI-1640, 10% v/v FBS, penicillin-streptomycin, supplemented with 2 mM L-ananyl-Lglutamine, 0.1 mM non-essential amino acids (#M7145-100ML, Sigma), and 1 mM sodium pyruvate (#11360070, Gibico™). All formulated cell culture media were sterilized by filtration (#569-0020, ThermoFisher) before use. Cells were cultured in cell culture flasks (430641U, Corning®) or dishes (#12-556-003, Thermo Scientific™) at 37 °C in a moisturized incubator with 5% CO_2.

CRT and HMGB1 Quantification by Flow Cytometry and ELISA:

A half-million CT26 cells were seeded in 12-well plates overnight in complete RPMI-1640 medium (2 mL/well). Doxorubicin (DOX), mitoxantrone (MTO), and oxaliplatin (OXA) were added to the cells at 1 and 10 μM for 24 h. One mL of supernatant was withdrawn from each well and centrifuged (800 rcf × 7 min) to remove dead cells and debris, before storage at −80 °C. The stored culture medium was subsequently used for HMGB1 analysis, using an ELISA kit as per manufacturer's instructions (#ST51011, Tecan IBL International).

For CRT analysis, CT26 cells were gently washed in PBS three times to harvest the lightly adhering dying or dead cells. Cells that remain attached were trypsinized (#25200056, Gibico™), centrifuged (400 rcf × 7 min), and combined with the lightly adhering cells. The combined cell pellets were washed once in a chilled cell staining buffer (#420201, BioLegend®) prior to antibody staining. Cells were then re-suspended in 100 μL of anti-CRT solution (#PA3-900, ThermoFisher, 1: 50 dilution) and incubated at room temperature for 30 min with intermittent vortexing. The stained cells were washed and re-suspended in 100 μL Alexa-405 labeled anti-IgG solution (A-31556, ThermoFisher, 1: 150 dilution) and incubated in the dark at room temperature (RT). The cell sample was then washed 3 times before resuspension in 1 mL staining buffer. The Live/Dead™ Fixable Green Dead Cell Staining Kit (#L23101, ThermoFisher) dye was reconstituted in DMSO and added to the suspended cells (1: 1000 v/v), incubated in the dark at RT before washing in staining buffer. The stained cells were fixed in 1 mL 4% paraformaldehyde for 15 min, washed and re-suspended in 200 μL staining buffer, and transferred into a 96-well plate for flow cytometry analysis (Attune NxT Flow Cytometer, ThermoFisher), using FlowJo™ v10 software. The data were expressed as the fold change in the percentage of CRT positive cells compared to the untreated control.

Synthesis of Cholesteryl-IND (Chol-IND):

The synthesis procedure for Chol-IND was designed and developed in-house. The first batch was synthesized at a small (−100 mg) scale to produce the first liposomal formulation and then outsourced to a CRO to produce a 5-gram batch, which according to HPLC, ^{1}H-NMR, and mass spectroscopy was 99% pure and in conformity with our analysis. Briefly, indoximod/IND (5 g, 1 eq, #452483, Sigma) and $NaHCO_3$ (5.77 g, 3 eq) was added into ice-cold THF (50% v/v in H_2O, 300 mL). Di-tert-butyl dicarbonate (5.25 g, 1.05 eq, #34460, Sigma) was dissolved in THF, then added drop-wise to the IND suspension. The reaction mixture was stirred for 12 h at RT and monitored by LCMS (Boc-IND: m/z = 341.1 [M+Na]+). THF was removed from the reaction mixture, and the remaining aqueous phase was extracted with ethyl acetate (EtOAc). The extracted aqueous phase was acidified (pH = 3 by citrate solution) to precipitate Boc-IND. The precipitated Boc-IND was recovered by filtration and dried under vacuum without further purification. Cholesterol conjugation to Boc-IND was carried out by Steglich esterification.[57]

In brief, Boc-IND (6.5 g, 1 eq), DMAP (247 mg, 0.1 eq), cholesterol (9.4 g, 1.2 eq), EDC.HCl (4.66 g, 1.2 eq) and TEA (4.1 g, 2 eq) were added into ice-cold CH_2Cl_2 (60 mL). The reaction mixture was stirred at RT for 12 h and monitored by LCMS (Chol-IND-Boc m/z = 687.4 $[M+H]^+$). The reaction mixture was poured into water and further extracted

with CH_2Cl_2. The combined CH_2Cl_2 extract was washed with brine in a separation funnel. Residual water in the organic solvent extract was absorbed by Na_2SO_4, and removed by filtration. The organic phase was concentrated and purified by flash chromatography (TLC solvent = Et_2O: EtOAc 5: 1, R_f = 0.7) to obtain cholesteryl-IND-Boc (Chol-IND-Boc). Chol-IND-Boc (8.7 g, 1 eq) was then dissolved in CH_2Cl_2 (100 mL) prior to the addition of TFA (9.38 mL, 10 eq, #8.08260, Sigma) at RT, stirred for 2 h and monitored by LCMS (Chol-IND-NH_3^+ m/z = 587.3 $[M+H]^+$). The reaction solvents were removed to obtain reaction crudes, which was further purified by prep-HPLC to obtain Chol-IND-$NH_3^+TFA^-$ (3.40 g, TFA salt). Amberlyst A-26 (20.0 g, #542571, Sigma) ion-exchange resin was added to Chol-IND-$NH_3^+TFA^-$ in CH_2Cl_2 (150 mL) and stirred at RT for 16 h. The insoluble resin was removed by filtration. The filtrate was concentrated to give the reaction crude, which was triturated with Et_2O (100 mL) and EtOAc (2 mL) at RT for 1 h to afford the Chol-IND (-NH_2, as free base). ^1H NMR and high-resolution mass spectroscopy spectra data for the reaction intermediates, *i.e.,* Boc-IND, Chol-IND-Boc, and Chol-IND, are available in Figure 3C and online (Figure S1).

Liposome Manufacturing by a Lipid Film Hydration Method for Lipid Batches of <30 mg.

All lipids required for liposome synthesis, *i.e.,* DSPC (#850365), Chol (#700000), CHEMS (#850524), DSPE-PEG_{2kDa} (#880120), were purchased from Avanti Polar Lipids. Lipids were prepared as stock solutions at 5 mg/mL in $CHCl_3$: MeOH = 4 : 1 (v/v) and stored at −20°C before use. To make the liposomes, the lipid stock solutions were warmed to room temperature and transferred into a round bottom flask using glass syringes (Hamilton). Organic solvents were carefully removed using a rotary evaporator to allow the deposition of a uniform, thin lipid film in a round bottom flask while drying under compressed nitrogen. The film quality was visually inspected and then rehydrated in a 100 mM citric acid-sodium citrate buffer solution (pH 4) at 65°C in a water bath to keep the lipid concentration < 20 mM. The hydrated suspension was dispersed by vortexing to yield a milky liposomal suspension. Liposomes were extruded 10 times, using benchtop extruders (#61000, Avanti and #LF-50, Avestin, Inc.) to pass the liposomes through series of polycarbonate filters (Whatman® Nuclepore filters) with a progressive decrease in pore sizes (1000 nm, 800 nm, 400 nm, 200 nm, and 100 nm). This ultimately brought the liposome size down to 100-120 nm before storage in sterilized containers.

Larger Scale Liposome Manufacturing by a Reverse-Phase Evaporation Method (to replace step 2 in the lipid film hydration method, as shown in Figure S14).

This method was used to make larger liposome batches of ~150 mg for the use in multiple parallel tumor models, described in Figure 9. A previously reported reverse-phase evaporation method was used to accomplish homogeneous mixing of the larger lipid content, as illustrated in Figure S14.[72, 73] In brief, the lipid powders were dispersed in $CHCl_3/Et_2O$ (6 mL, 1: 1 v/v, MeOH/EtOH-free) in a round bottom flask, followed by adding 1.5 mL of a 100 mM citric acid/sodium citrate buffer (pH 4). The bi-phase and phase-separated solution were sonicated for 30 min in a bath sonicator at 45°C, yielding a milky w/o emulsion. Organic solvents were gradually removed from the emulsion, using a rotary evaporator at 45°C for 2-3 h. The drying emulsion transitioned to a white gel-like phase, before breaking

into an aqueous liposomal dispersion. Liposome exclusion was performed as described above.

MTO Encapsulation, Using a Remote Loading Technique.

Liposomal transmembrane loading of MTO was achieved through a previously published method.[39] In brief, extruded liposomes in the citric acid-sodium citrate buffer (pH 4) were loaded onto disposable single-use size-exclusion desalting columns (PD10 columns, GE Healthcare) and eluted with sterilized PBS buffer (#BP2944100, Fisher Scientific). This established liposomes with a transmembrane pH gradient (exterior = pH 7.4, interior = pH 4). Mitoxantrone dihydrochloride (MTO, #M6545, Sigma) solution in PBS was added at 10% and 15% (w/w drug/lipid) for the L-MTO/IND) and L-MTO nanocarriers, respectively. Following incubation at 65°C for 1 h, the solution was cooled to RT before removing the non-encapsulated MTO across Sephadex-G25 columns in a biosafety cabinet. The elution profile of the synthesized liposomes was determined by a Stewart assay.[114] The elution profile, calibration curve, and the quantity of non-encapsulated MTO in the PD10 column were established by UV measurement (λ_{max}: 610 nm) of MTO standard solutions and the eluents. The encapsulated MTO was calculated by subtracting the free from the feeding MTO concentration. The maximum MTO loading was determined to be 10% and 15% (MTO/lipid %w/w, initial MTO feeding = 18% w/w) for L-MTO and L-MTO/IND, respectively. The final MTO loading levels were 9.7% w/w (feeding = 18% w/w, EE% = 54% m/m) and 9.1% w/w (feeding = 10%, EE% = 91%) for L-MTO and L-MTO/IND, respectively. All the liposomes were subjected to physicochemical characterization before usage.

Physicochemical Characterization of Liposomes.

Dynamic light scattering (ZetaPALS, Brookhaven Instrument) was used to characterize the colloidal liposomes properties. Size distribution was performed with 5 mM liposomes, diluted 1: 1000 in citric acid/sodium citrate buffer (pH 4) or PBS (pH 7.4). Zeta potential was measured by diluting 5 mM liposomes, 1: 1000 in de-ionized water. To assess morphology, liposomes (2.5 μL at 2 mg/mL) were loaded onto TEM grids (#661-200-CU-100, Ted Pella), cleaned with easiGlow™ (Ted Pella), then cooled in liquid ethane (Vitrobot Mark IV, ThermoFisher). The frozen liposomes were visualized using a cryoEM (TF20 FEI Tecnai-G2, 300 kV in the low dose mode).

Western Blotting to Determine IDO-1 Expression:

In order to assess IDO-1 expression in different cancer cell lines during treatment with IFN-γ, cells were seeded in 6-well plates and exposed to IFN-γ at 100 ng/mL (#485-MI-100, R&D Systems) for 24 h. After washing, cells were washed and disrupted in a RIPA lysis buffer (#20-188, Millipore), supplemented with protease inhibitor (#4693159001, Roche) and phosphatase inhibitor cocktails (#sc-45-44, Santa Cruz) for Western Blot analysis. The protein concentrations of the lysates were determined with a Bradford assay (Quick Start™, Bio-Rad), before incubation with SDS sample buffer (20-30 μg/sample, #LC2676, ThermoFisher) and heating to 95°C for 2 min. The samples were electrophoresed through a 10-20% tris-glycine SDS-PAGE gel, before transfer to a PVDF membrane (#IPVH00010, Millipore). The membrane was blocked with filtered (Falcon 70μm cell strainer, #352350,

Corning) 5% non-fat milk (#M17200. Research Products International)/TBST blocking buffer, before being overlaid with primary (4°C, overnight) and HRP-conjugated secondary antibodies (1 h at RT). The blots were developed using an ECL substrate (#32109, ThermoFisher) and visualized on x-ray films (Bioland Scientific). The results were analyzed using ImageJ v1.5.2 software (NIH, USA). The primary antibodies were used to stain vinculin (#4560, CST, 1: 1000 dilution), IDO-1 (#51851S, CST, 1: 1000 dilution) and GAPDH (#ab8245, Abcam, 1: 5000 dilution). The secondary was an HRP-conjugated antibody (#7074 and #7076, CST, 1: 1000 dilution).

Western Blotting to Determine Chol-IND Efficacy *in Vitro:*

In order to compare the efficacy of liposomal Chol-IND (L-IND) to free IND, CT26 cells were seeded in 6-well plate and grown until confluent. Cells were pre-treated with IFN-γ at 100 ng/mL overnight to stimulate IDO expression. Cells were gently washed three times then incubated in tryptophan-free and serum-free media (custom made, Gibico), supplemented with IND or L-IND at 1, 10, and 50 μM for 6 hours. Western blotting was performed using the methods mentioned in the previous section. The PVDF membranes were blocked with 5% non-fat milk/TBST buffer; membrane containing S6K, and P-S6K were blocked with 5% BSA (#3116964001, Roche)/TBST buffer. Primary antibodies were used to bind vinculin (#4560, CST, 1: 1000 dilution), S6K (#9209, CST, 1: 1000 dilution), P-S6K (#9205S, CST, 1: 1000 dilution). The secondary was an HRP-conjugated antibody (#7074 CST, phospho-p70S6K 1: 2500 dilution, 1: 1000 dilution for p70S6K and phospho-p70S6K).

Stability Studies for Liposomes:

To evaluate the L-MTO/IND stability after storage, the liposomes were freshly prepared and stored at 4°C for up to 3-month. Liposome morphology was observed using TF20 FEI Tecnai-G2 cryoEM. The hydrodynamic size and zeta potential of the L-MTO/IND were measured by Brookhaven ZetaPALS zeta potential & particle size analyzer. To detect the IND release, 500 μL of L-MTO/IND suspension was centrifuged at 3,000 g for 15 min using an Amicon filter unit (cutoff: 30 kDa). The filtrate was used to quantify free IND in a PerkinElmer Altus HPLC with a Brownlee SPP 2.7 μm C18 Columns (4.6 X 150 mm). The HPLC was performed using a mixture of HPLC grade water and acetonitrile (H_2O: acetonitrile = 85:15 v/v, flow rate = 1 mL/min, temperature = 25°C). Ten microliters of the filtrate were injected into the column, and the IND concentration in the eluate was measured by the Altus A-10 UV detector at 290 nm. To detect the released MTO, 500 μL of L-MTO/IND suspension was centrifuged at 3,000 g for 15 min using Amicon ultra 0.5 mL (cutoff: 30 kDa) centrifugal filter unit. The filtrate was used to quantify the free MTO concentration by Spectramax M5e multi-mode microplate reader at 607/685 nm excitation and emission wavelengths.

Assessment of the Variation of the Liposomal ζ-potential Over the pH Range, 7.4 to 3.8.

L-MTO and L-MTO/IND were initially prepared in PBS, as described previously. The PBS was replaced by pH 7.4 citric acid sodium phosphate (Na_2HPO_4) buffer using a pre-packed size exclusion column (Sephadex G-25/PD10). The pH of the buffer was then adjusted by sequentially increasing the 0.1 M citrate to 0.2 M Na_2HPO_4 ratio from 9.15: 90.85 (pH 7.4)

to 67.80: 32.20 (pH 3.8). Liposomes were ice-chilled during to titration process and vortexed for 30 seconds before 100X diluted in deionized water for ζ-potential measurements.

Establishing syngeneic tumor models in Balb/c mice.

Subcutaneous injections were performed in female Balb/c mice (Charles Rivers) that were maintained under pathogen-preconditions in the UCLA vivarium. All animal experiment protocols were approved by the UCLA Animal Research Committee. For subcutaneous tumor models, each animal received the delivery of 0.7M CT26, EMT6, RENCA, and 4T1 cells in a 100 μL Matrigel® (50% v/v in PBS, #CB35428, Corning) subcutaneously into the right flank. The 4T1 orthotopic model was established by inoculating 0.7 M 4T1 cells (50μL, 50% v/v Matrigel® in PBS) subcutaneously into the 2nd right mammary fat pad of female Balb/c mice. Tumor growth was monitored daily by a digital caliper. Tumor size in mm^3 was estimated by $(W^2 \times L)/2$.[115] Treatments were given through tail vein IV injection when tumor size reached 100~150 mm^3. Injections were given every three days for a total of four injections.

Visualizing MTO Released From Liposomes *in Vitro:*

L-MTO and L-MTO/IND (2 μL x 0.3 mg MTO/mL) were loaded into a black-walled transparent bottom 96-well plate (#353219, BD Falcon). The liposomes were diluted 100 × in pH 4 citric acid sodium citrate buffer, pH 7.4 PBS, or 50% fetal bovine serum in PBS, respectively, before incubation at 37°C for 48 h. Triton X-100 (2% v/v) was used to disrupt the liposomes to ensure MTO dissolution.[72] After the incubation, the plate was imaged by an IVIS imager (Excitation filter: 675 nm; Emission filter: Cy5.5) then analyzed by Living Image® software (PerkinElmer, version 4.5).

Visualizing Liposomal Released MTO *in Vivo*:

The experiment was carried out in CT26.WT tumor-bearing Balb/c mice. The biodistribution of free MTO, L-MTO, and L-MTO/IND was assessed by injecting these formulations IV at a dose equivalent of 3 mg/kg MTO ($n = 3$). Mice were sacrificed after 24 h, and 48 h and *ex vivo* MTO fluorescence images were obtained of the expanded tumors, hearts, livers, spleens, lungs, and kidneys, using an IVIS imager (Excitation filter: 675 nm; Emission filter: Cy5.5). The organs from untreated animals were used to establish subtractable autofluorescence. MTO fluorescence was obtained by Living Image® software (PerkinElmer, version 4.5). Data were expressed as fold-change in fluorescence intensity (average radiant efficiency [p/s/cm^2/sr] / [μW/cm^2]) in organs of animals treated with encapsulated *versus* free MTO.

Assessment of the Pharmacokinetics of Free MTO and Liposomal MTO Formulations:

The experiment was carried out in CT26.WT tumor-bearing Balb/c mice 14 days after tumor inoculation. The serum pharmacokinetic profiles of free MTO, L-MTO, and L-MTO/IND were assessed by giving a single IV bolus injection at an MTO equivalent dose at 3 mg/kg ($n = 3$/time point). Blood collections were performed at 5 min, 15 min, 30 min, 1 h, 2 h, 4 h, 24 h, and 48 h post-injection. Blood was collected using serum separation tubes (#365967, BD Microtainer® SST™) then centrifuged at 10,000 rpm to isolate the drug-containing serum.

The hydrochloride salt of the MTO in the isolated serum was naturalized by saturated sodium bicarbonate ($NaHCO_3$, 100μL). Free-base MTO was extracted by $CHCl_3$ (100 μL × 3). The $CHCl_3$ extracts were combined (300 μL) and back-extracted using 0.1N HCl (100 μL × 2) to obtain water-soluble hydrochloride salted MTO suitable for HPLC analysis. The HPLC method for MTO analysis is covered above in the stability study. Tumors harvested at 24 h and 48 h post-injection were chopped up, weighted (0.3-0.5 g), loaded into tissue homogenization tubes (#15350153, 1. 4mm ceramic beads, Fisher Scientific) in 1 mL saturated $NaHCO_3$ solution, then homogenized *via* a bead mill (#15340164, Fisher Scientific). The homogenates were recovered and mixed with 1 mL crash solution (MeOH: MeCN = 1:1 v/v), stored at 4°C for 24 h then centrifuged at 10,000 rcf. The supernatants were collected and extracted by $CHCl_3$, followed by 0.1N HCl as described for serum MTO extraction, then analyzed by HPLC.

Therapeutic Efficacy and Survival Studies.

Tumor-bearing animals were randomly grouped when the tumor sizes reached 100~150 mm^3 (~day 8 post-inoculation). The first efficacy study was carried out in the CT26 model. CT26 tumor-bearing mice were randomly assigned to 3 groups, *i.e.,* untreated control (saline), L-MTO (without IND), and L-MTO/IND. Group sizes consisted of 6-10 animals. Treatment was IV administered *via* the tail vein on days 8, 11, 14, and 17. The injection doses of MTO and IND were 3 mg/kg and 2.8 mg/kg, respectively. Tumor growth was monitored daily by a digital caliper. Following animal sacrifice on day 23, tumors were harvested, weighed, and formalin-fixed for immunohistochemistry studies. A similar approach (dosimetry, administration frequency, dose) was used for determining survival outcomes in the CT26 model, except that the animals were allowed to reach end-of-life, and the comparisons were made between untreated animals or animals treated with L-IND/MTO and L-MTO. Animals were euthanized when reaching endpoints such as spontaneous death or approaching moribund status (according to particle criteria). To demonstrate the broader utilization of our technology, L-IND/MTO, and L-MTO were also tested in the EMT6 (breast cancer), RENCA (renal cancer), and 4T1 (breast cancer) models. Similar to the study in the CT26 model, the tumor-bearing mice received L-IND/MTO at MTO and IND at 3 mg/kg and 2.8 mg/kg per injection, respectively. Treatment frequency was similar to the CT26 efficacy experiment. Animals were sacrificed on day 23. The efficacy and survival studies were repeated in an orthotopic 4T1 model. The injection dose and treatment frequency were identical to all previous studies. However, the total number of IV injections reduced from 4 to 3 injections, due to the MTD limitation of free MTO (included as the free-drug control).

Immunohistochemistry (IHC).

Formalin-fixed tumors were processed at the UCLA Translational Pathology Core Laboratory (TPCL) for paraffin embedding, sectioning, and staining. In brief, tissue sections were stained for overnight at 4°C for primary antibodies or 30 min for HRP-conjugated secondary antibodies at RT. The signal was detected using an anti-rabbit HRP polymer. All sections were visualized with DAB (diaminobenzidine), counterstained with hematoxylin. Slides were digitally scanned using an Aperio AT Turbo Digital Pathology Scanner (Leica Biosystems). Primary antibodies, comprising: (i) anti-CD8 (#14-0808; 1: 100), anti-NKp46

(#PA5-79720; 1: 50), and anti-Fop33 (#13-5573; 1: 500) were purchased from ThermoFisher; (ii) anti-CRT (#ab2907, 1: 200), anti-HMGB1 (#ab18256, 1: 200), anti-perforin (#ab16074, 1:100), anti-granzyme B (#ab4059, 1: 100), and anti-IFN-γ (#ab9697, 1: 200) were purchased from Abcam; (iii) anti-IDO (#122402, 1: 100) was from BioLegend; (iv) anti-LC3B (NB100-2200, 1: 100) was from Nanotools. Secondary rabbit anti-rat antibodies from Vector Labs (#AI-4001) were used two detect the primary staining antibodies for Perforin, CD8a, Foxp3, and IDO (#AI-4001, Vector Labs). The HRP-labelled polymeric anti-rabbit antibody was from Agilent (#K4003). Quantitative IHC analysis was performed using Aperio ImageScope software v12 (Leica). For quantification of the IHC staining intensity of CRT, HMGB1, LC3B, perforin, granzyme B, and IDO levels, the positive pixel count plugin (v9) for ImageScope software was used. The positivity index was derived by determining the number of positive pixels/total pixels per field, and then normalized to untreated samples (3-5 fields/tumor × 6 tumors/treatment). The number of $CD8^+$, $NKp46^+$, and $Foxp3^+$ cells was determined by manual counting (*i.e.,* averaged counting from 3-5 fields/tumor, $n = 6$ tumors/group).

Multiplex IHC

Unstained IHC slides from standard IHC preparations were dewaxed (xylene 3 washes × 10 min), gradually rehydrated in EtOH solutions (100% 5 min, 95% 5 min, 70% 2 min), boiled in AR buffer in a microwave, then cooled to RT. Tissues were blocked in PerkinElmer antibody diluent buffer in a humidified chamber at RT for 10 min before overnight staining with primary antibodies, then stained 30 min with HRP-labelled polymeric anti-rabbit antibody. Signal amplification was achieved using Opal™ fluorophore working solutions (1: 100 dilution) at RT for 10 min then microwaved. The primary-secondary-HRP complex was stripped before repeating the steps for multiplexing staining, then mounting the slides with DAPI for 5 min. Slides were visualized using PhenoCharts v1.0.2 (Akoya Bioscience). The antibody diluent (#ARD100), amplification diluent (FP1498), Opal-520-FITC (#FP148700, 1: 100 v/v for perforin), Opal-570-TRITC (#FP148800,1: 200 v/v for NKp46, Opal-480 (#14-0808, 1:200 v/v for CD8) AR6 and AR9 buffer (AR600/900), and Opal-DAPI (FP1490) were purchased form Akoya Bioscience.

Statistical Analysis.

Differences among groups were estimated by the analysis of variance (ANOVA, post hoc = Tukey's or Dunnett's T3 multiple comparisons test). Kaplan Meier survival curves were compared using the Log-rank Mantel-Cox test (GraphPad Prism v8.4.2). Results were presented as mean ± standard deviation (S.D.), representing at least three independent experiments. Statistical significance was set at $*p < 0.05$; $**p < 0.01$; $***p < 0.001$, and $****p < 0.001$, as indicated in the figure legends.

Supplementary Material

Refer to Web version on PubMed Central for supplementary material.

Acknowledgments

Research reported in this publication was supported by the National Cancer Institute of the National Institutes of Health under Award Numbers, U01CA198846 and 1R01CA247666-01A1. We thank the Translational Pathology Core Laboratory (TPCL) at UCLA Jonsson Comprehensive Cancer Center for IHC staining, the Electron Imaging Center for Nanomachines the use of EM instruments at, the Molecular Instrumentation Center for NMRs and Mass Spectrometry, the CNSI Advanced Light Microscopy/Spectroscopy Shared Facility for confocal fluorescent microscopy.

References

1. Galluzzi L; Vitale I; Warren S; Adjemian S; Agostinis P; Martinez AB; Chan TA; Coukos G; Demaria S; Deutsch E; Draganov D; Edelson RL; Formenti SC; Fucikova J; Gabriele L; Gaipl US; Gameiro SR; Garg AD; Golden E; Han J; Harrington KJ; Hemminki A; Hodge JW; Hossain DMS; Illidge T; Karin M; Kaufman HL; Kepp O; Kroemer G; Lasarte JJ; Loi S; Lotze MT; Manic G; Merghoub T; Melcher AA; Mossman KL; Prosper F, Rekdal Ø; Rescigno M; Riganti C; Sistigu A; Smyth MJ; Spisek R; Stagg J; Strauss BE; Tang D; Tatsuno K; van Gool SW; Vandenabeele P; Yamazaki T; Zamarin D; Zitvogel L; Cesano A; Marincola FM, Consensus Guidelines for the Definition, Detection and Interpretation of Immunogenic Cell Death. J. for Immunother. Cancer 2020, 8, e000337.
2. Kroemer G; Galluzzi L; Kepp O; Zitvogel L, Immunogenic Cell Death in Cancer Therapy. Annu. Rev. Immunol 2013, 31, 51–72. [PubMed: 23157435]
3. Pol J; Vacchelli E; Aranda F; Castoldi F; Eggermont A; Cremer I; Sautès-Fridman C; Fucikova J; Galon J; Spisek R; Tartour E; Zitvogel L; Kroemer G; Galluzzi L, Trial Watch: Immunogenic Cell Death Inducers for Anticancer Chemotherapy. Oncoimmunology 2015, 4, e1008866–e 1008866. [PubMed: 26137404]
4. Sukkurwala AQ; Adjemian S; Senovilla L; Michaud M; Spaggiari S; Vacchelli E; Baracco EE; Galluzzi L; Zitvogel L; Kepp O; Kroemer G, Screening of Novel Immunogenic Cell Death Inducers Within the NCI Mechanistic Diversity Set. Oncoimmunology 2014, 3, e28473–e28473. [PubMed: 25050214]
5. Golden EB; Apetoh L, Radiotherapy and Immunogenic Cell Death. Semin. Radiat. Oncol 2015, 25, 11–17. [PubMed: 25481261]
6. Galluzzi L; Kepp O; Kroemer G, Enlightening the Impact of Immunogenic Cell Death in Photodynamic Cancer Therapy. EMBO J. 2012, 31, 1055–1057. [PubMed: 22252132]
7. Obeid M; Panaretakis T; Joza N; Tufi R; Tesniere A; van Endert P; Zitvogel L; Kroemer G, Calreticulin Exposure Is Required for the Immunogenicity of γ-Irradiation and UVC Light-Induced Apoptosis. Cell Death Differ. 2007, 14, 1848–1850. [PubMed: 17657249]
8. Obeid M; Tesniere A; Ghiringhelli F; Fimia GM; Apetoh L; Perfettini J-L; Castedo M; Mignot G; Panaretakis T; Casares N; Métivier D; Larochette N; van Endert P; Ciccosanti F; Piacentini M; Zitvogel L; Kroemer G, Calreticulin Exposure Dictates the Immunogenicity of Cancer Cell Death. Nature Medicine 2007, 13, 54–61.
9. Tesniere A; Schlemmer F; Boige V; Kepp O; Martins I; Ghiringhelli F; Aymeric L; Michaud M; Apetoh L; Barault L; Mendiboure J; Pignon JP; Jooste V; van Endert P; Ducreux M; Zitvogel L; Piard F; Kroemer G, Immunogenic Death of Colon Cancer Cells Treated With Oxaliplatin. Oncogene 2010, 29, 482–491. [PubMed: 19881547]
10. Green DR; Ferguson T; Zitvogel L; Kroemer G, Immunogenic and Tolerogenic Cell Death. Nat. Rev. Immunol 2009, 9, 353–363. [PubMed: 19365408]
11. Kelland L, The Resurgence of Platinum-Based Cancer Chemotherapy. Nat. Rev. Cancer 2007, 7, 573–584. [PubMed: 17625587]
12. Galluzzi L; Buqué A; Kepp O; Zitvogel L; Kroemer G, Immunogenic Cell Death in Cancer and Infectious Disease. Nat. Rev. Immunol 2017, 17, 97–111. [PubMed: 27748397]
13. Chattopadhyay PK; Betts MR; Price DA; Gostick E; Horton H; Roederer M; De Rosa SC, The Cytolytic Enzymes Granyzme A, Granzyme B, and Perforin: Expression Patterns, Cell Distribution, and Their Relationship to Cell Maturity and Bright CD57 Expression. J. Leukoc. Biol 2009, 85, 88–97. [PubMed: 18820174]

14. Voskoboinik I; Whisstock JC; Trapani JA, Perforin and Granzymes: Function, Dysfunction and Human Pathology. Nat. Rev. Immunol 2015, 15, 388–400. [PubMed: 25998963]
15. Trapani JA; Smyth MJ, Functional Significance of the Perforin/Granzyme Cell Death Pathway. Nat. Rev. Immunol 2002, 2, 735–747. [PubMed: 12360212]
16. Chanvillard C; Millward JM; Lozano M; Hamann I; Paul F; Zipp F; Dörr J; Infante-Duarte C, Mitoxantrone Induces Natural Killer Cell Maturation in Patients with Secondary Progressive Multiple Sclerosis. PLoS One 2012, 7, e39625–e39625. [PubMed: 22768101]
17. Zingoni A; Fionda C; Borrelli C; Cippitelli M; Santoni A; Soriani A, Natural Killer Cell Response to Chemotherapy-Stressed Cancer Cells: Role in Tumor Immunosurveillance. Front. Immunol 2017, 8, 1194–1194. [PubMed: 28993779]
18. Smyth MJ; Thia KYT; Cretney E; Kelly JM; Snook MB; Forbes CA; Scalzo AA, Perforin Is a Major Contributor to NK Cell Control of Tumor Metastasis. J. Immunol 1999, 162, 6658–6662. [PubMed: 10352283]
19. Rodallec A; Sicard G; Fanciullino R; Benzekry S; Lacarelle B; Milano G; Ciccolini J, Turning Cold Tumors Into Hot Tumors: Harnessing the Potential of Tumor Immunity Using Nanoparticles. Expert Opin. Drug Metab. Toxicol 2018, 14, 1139–1147. [PubMed: 30354685]
20. Duan Q; Zhang H; Zheng J; Zhang L, Turning Cold into Hot: Firing Up the Tumor Microenvironment. Trends Cancer 2020, 6, 605–618. [PubMed: 32610070]
21. Binnewies M; Roberts EW; Kersten K; Chan V; Fearon DF; Merad M; Coussens LM; Gabrilovich DI; Ostrand-Rosenberg S; Hedrick CC; Vonderheide RH; Pittet MJ; Jain RK; Zou W; Howcroft TK; Woodhouse EC; Weinberg RA; Krummel MF, Understanding the Tumor Immune Microenvironment (TIME) for Effective Therapy. Nature Medicine 2018, 24, 541–550.
22. Bayraktar S; Batoo S; Okuno S; Gluck S, Immunotherapy in Breast Cancer. J. Carcinog 2019, 18, 2–2. [PubMed: 31160888]
23. Doo DW; Norian LA; Arend RC, Checkpoint Inhibitors in Ovarian Cancer: A Review of Preclinical Data. Gynecol. Oncol. Rep 2019, 29, 48–54. [PubMed: 31312712]
24. Rios-Doria J; Durham N; Wetzel L; Rothstein R; Chesebrough J; Holoweckyj N; Zhao W; Leow CC; Hollingsworth R, Doxil Synergizes with Cancer Immunotherapies to Enhance Antitumor Responses in Syngeneic Mouse Models. Neoplasia 2015, 17, 661–70. [PubMed: 26408258]
25. Walters AA; Wang JT-W; Al-Jamal KT, Evaluation of Cell Surface Reactive Immuno-Adjuvant in Combination with Immunogenic Cell Death Inducing Drug for *In Situ* Chemo-Immunotherapy. J. Controlled Release 2020, 322, 519–529.
26. Shmeeda H; Amitay Y; Gorin J; Tzemach D; Mak L; Stern ST; Barenholz Y; Gabizon A, Coencapsulation of Alendronate and Doxorubicin in Pegylated Liposomes: A Novel Formulation for Chemoimmunotherapy of Cancer. J. Drug Targeting 2016, 24, 878–889.
27. Mbongue JC; Nicholas DA; Torrez TW; Kim N-S; Firek AF; Langridge WHR, The Role of Indoleamine 2, 3-Dioxygenase in Immune Suppression and Autoimmunity. Vaccines 2015, 3, 703–729. [PubMed: 26378585]
28. Castro F; Cardoso AP; Gonçalves RM; Serre K; Oliveira MJ, Interferon-Gamma at the Crossroads of Tumor Immune Surveillance or Evasion. Front. Immunol 2018, 9, 847–847. [PubMed: 29780381]
29. Prendergast GC; Smith C; Thomas S; Mandik-Nayak L; Laury-Kleintop L; Metz R; Muller AJ, Indoleamine 2,3-Dioxygenase Pathways of Pathogenic Inflammation and Immune Escape in Cancer. Cancer Immunol. Immunother 2014, 63, 721–735. [PubMed: 24711084]
30. Mojic M; Takeda K; Hayakawa Y, The Dark Side of IFN-γ: Its Role in Promoting Cancer Immunoevasion. Int. J. Mol. Sci 2017, 19 (1), 89.
31. Labadie BW; Bao R; Luke JJ, Reimagining IDO Pathway Inhibition in Cancer Immunotherapy *via* Downstream Focus on the Tryptophan–Kynurenine–Aryl Hydrocarbon Axis. Clin. Cancer Res 2019, 25, 1462–1471. [PubMed: 30377198]
32. Topalian SL; Taube JM; Pardoll DM, Neoadjuvant Checkpoint Blockade for Cancer Immunotherapy. Science 2020, 367, eaax0182. [PubMed: 32001626]
33. Keung EZ; Ukponmwan EU; Cogdill AP; Wargo JA, The Rationale and Emerging Use of Neoadjuvant Immune Checkpoint Blockade for Solid Malignancies. Ann. Surg. Oncol 2018, 25, 1814–1827. [PubMed: 29500764]

34. Nowicki TS; Hu-Lieskovan S; Ribas A, Mechanisms of Resistance to PD-1 and PD-L1 Blockade. Cancer J. 2018, 24, 47–53. [PubMed: 29360728]
35. Jenkins RW; Barbie DA; Flaherty KT, Mechanisms of Resistance to Immune Checkpoint Inhibitors. Br. J. Cancer 2018, 118, 9–16. [PubMed: 29319049]
36. Gao J; Deng F; Jia W, Inhibition of Indoleamine 2,3-Dioxygenase Enhances the Therapeutic Efficacy of Immunogenic Chemotherapeutics in Breast Cancer. J. Breast Cancer 2019, 22, 196–209. [PubMed: 31281723]
37. Meng X; Du G; Ye L; Sun S; Liu Q; Wang H; Wang W; Wu Z; Tian J, Combinatorial Antitumor Effects of Indoleamine 2,3-Dioxygenase Inhibitor NLG919 and Paclitaxel in a Murine B16-F10 Melanoma Model. Int. J. Immunopathol. Pharmacol 2017, 30, 215–226. [PubMed: 28604143]
38. Li C; Cui J; Wang C; Li Y; Zhang H; Wang J; Li Y; Zhang L; Zhang L; Guo W; Wang Y, Encapsulation of Mitoxantrone Into Pegylated SUVs Enhances Its Antineoplastic Efficacy. Eur. J. Pharm. Biopharm 2008, 70, 657–665. [PubMed: 18582570]
39. Lim HJ; Masin D; Madden TD; Bally MB, Influence of Drug Release Characteristics on the Therapeutic Activity of Liposomal Mitoxantrone. J. Pharmacol. Exp. Ther 1997, 281, 566–573. [PubMed: 9103545]
40. Li C; Zhao X; Deng C; Wang C; Wei N; Cui J, Pegylated Liposomal Mitoxantrone is More Therapeutically Active Than Mitoxantrone in L1210 Ascitic Tumor and Exhibits Dose-Dependent Activity Aaturation Effect. Int. J. Pharm 2014, 460, 165–172. [PubMed: 24148664]
41. Chang CW; Barber L; Ouyang C; Masin D; Bally MB; Madden TD, Plasma Clearance, Biodistribution and Therapeutic Properties of Mitoxantrone Encapsulated in Conventional and Sterically Stabilized Liposomes After Intravenous Administration in BDF1 Mice. Br. J. Cancer 1997, 75, 169–177. [PubMed: 9010021]
42. Liu Q; Chen F; Hou L; Shen L; Zhang X; Wang D; Huang L, Nanocarrier-Mediated Chemo-Immunotherapy Arrested Cancer Progression and Induced Tumor Dormancy in Desmoplastic Melanoma. ACS Nano 2018, 12, 7812–7825. [PubMed: 30016071]
43. Gilabert-Oriol R; Ryan GM; Leung AWY; Firmino NS; Bennewith KL; Bally MB, Liposomal Formulations to Modulate the Tumour Microenvironment and Antitumour Immune Response. Int. J. Mol. Sci 2018, 19, 2922.
44. Fan Y; Kuai R; Xu Y; Ochyl LJ; Irvine DJ; Moon JJ, Immunogenic Cell Death Amplified by Co-localized Adjuvant Delivery for Cancer Immunotherapy. Nano Lett. 2017, 17, 7387–7393. [PubMed: 29144754]
45. Kuai R; Yuan W; Son S; Nam J; Xu Y; Fan Y; Schwendeman A; Moon JJ, Elimination of Established Tumors With Nanodisc-Based Combination Chemoimmunotherapy. Sci. Adv 2018, 4, eaao1736. [PubMed: 29675465]
46. Fox EJ, Mechanism of Action of Mitoxantrone. Neurology 2004, 63, S15–18. [PubMed: 15623664]
47. Economides MP; McCue D; Borthakur G; Pemmaraju N, Topoisomerase II Inhibitors in AML: Past, Present, and Future. Expert Opin. Pharmacother 2019, 20, 1637–1644. [PubMed: 31136213]
48. Kieseier BC; Jeffery DR, Chemotherapeutics in the Treatment of Multiple Sclerosis. Ther. Adv. Neurol. Disord 2010, 3, 277–291. [PubMed: 21179618]
49. Obeid M, ERP57 Membrane Translocation Dictates the Immunogenicity of Tumor Cell Death by Controlling the Membrane Translocation of Calreticulin. J. Immunol 2008, 181, 2533–2543. [PubMed: 18684944]
50. Fox E; Oliver T; Rowe M; Thomas S; Zakharia Y; Gilman PB; Muller AJ; Prendergast GC, Indoximod: An Immunometabolic Adjuvant That Empowers T Cell Activity in Cancer. Front. Oncol 2018, 8, 370–370. [PubMed: 30254983]
51. Muggia FM; Fojo T, Platinums: Extending Their Therapeutic Spectrum. J. Chemother 2004, 16, 77–82.
52. Liu J; Cao X, Cellular and Molecular Regulation of Innate Inflammatory Responses. Cell. Mol. Immunol 2016, 13, 711–721. [PubMed: 27818489]
53. Workenhe ST; Pol JG; Lichty BD; Cummings DT; Mossman KL, Combining Oncolytic HSV-1 with Immunogenic Cell Death-Inducing Drug Mitoxantrone Breaks Cancer Immune Tolerance and Improves Therapeutic Efficacy. Cancer Immunol. Res 2013, 1, 309–319. [PubMed: 24777969]

54. Richard B; Launay-Iliadis MC; Iliadis A; Just-Landi S; Blaise D; Stoppa AM; Viens P; Gaspard MH; Maraninchi D; Cano JP Pharmacokinetics of Mitoxantrone in Cancer Patients Treated by High-Dose Chemotherapy and Autologous Bone Marrow Transplantation. Br. J. Cancer 1992, 65, 399–404. [PubMed: 1558794]

55. Ehninger G; Schuler U; Proksch B; Zeller K-P; Blanz J, Pharmacokinetics and Metabolism of Mitoxantrone A Review. Clin. Pharmacokinet 1990, 18 (5), 365–380. [PubMed: 2185907]

56. Maag H, Prodrugs of Carboxylic Acids. In Prodrugs: Challenges and Rewards Part 1, Stella VJ; Borchardt RT; Hageman MJ; Oliyai R; Maag H; Tilley JW, Eds. Springer New York: New York, NY, 2007; pp 703–729.

57. Neises B; Steglich W, Simple Method for the Esterification of Carboxylic Acids. Angew. Chem., Int. Ed. Engl 1978, 17, 522–524.

58. Metz R; Rust S; Duhadaway JB; Mautino MR; Munn DH; Vahanian NN; Link CJ; Prendergast GC, IDO Inhibits a Tryptophan Sufficiency Signal that Stimulates mTOR: A Novel IDO Effector Pathway Targeted by D-1-Methyl-Tryptophan. Oncoimmunology 2012, 1, 1460–1468. [PubMed: 23264892]

59. Tansi FL; Rüger R; Rabenhold M; Steiniger F; Fahr A; Hilger I, Fluorescence-Quenching of a Liposomal-Encapsulated Near-Infrared Fluorophore as a Tool for in Vivo Optical Imaging. J. Visualized Exp 2015, e52136–e52136.

60. Larimer BM; Bloch E; Nesti S; Austin EE; Wehrenberg-Klee E; Boland G; Mahmood U, The Effectiveness of Checkpoint Inhibitor Combinations and Administration Timing Can Be Measured by Granzyme B PET Imaging. Clin. Cancer Res 2019, 25, 1196–1205. [PubMed: 30327313]

61. Hou W; Zhang Q; Yan Z; Chen R; Zeh Iii HJ; Kang R; Lotze MT; Tang D, Strange Attractors: DAMPs and Autophagy Link Tumor Cell Death and Immunity. Cell Death Dis. 2013, 4, e966–e966. [PubMed: 24336086]

62. Michaud M; Martins I; Sukkurwala AQ; Adjemian S; Ma Y; Pellegatti P; Shen S; Kepp O; Scoazec M; Mignot G; Rello-Varona S; Tailler M; Menger L; Vacchelli E; Galluzzi L; Ghiringhelli F; di Virgilio F; Zitvogel L; Kroemer G, Autophagy-Dependent Anticancer Immune Responses Induced by Chemotherapeutic Agents in Mice. Science 2011, 334, 1573–1577. [PubMed: 22174255]

63. Saleiro D; Platanias LC, Intersection of mTOR and STAT Signaling in Immunity. Trends Immunol. 2015, 36, 21–29. [PubMed: 25592035]

64. Paolini R; Bernardini G; Molfetta R; Santoni A, NK Cells and Interferons. Cytokine Growth Factor Rev. 2015, 26, 113–120. [PubMed: 25443799]

65. Baginska J; Viry E; Berchem G; Poli A; Noman MZ; van Moer K; Medves S; Zimmer J; Oudin A; Niclou SP; Bleackley RC; Goping IS; Chouaib S; Janji B, Granzyme B Degradation by Autophagy Decreases Tumor Cell Susceptibility to Natural Killer-Mediated Lysis Under Hypoxia. Proc. Natl. Acad. Sci. U. S. A 2013, 110, 17450–17455. [PubMed: 24101526]

66. Brincks EL; Adams J; Wang L; Turner B; Marcinowicz A; Ke J; Essmann M; Mautino LM; Allen CV; Kumar S; Vahanian N; Link C; Mautino MR, Indoximod Opposes The Immunosuppressive Effects Mediated by IDO and TDO via Modulation of AhR Function and Activation of mTORC1. Oncotarget 2020, 11, 2438–2461. [PubMed: 32637034]

67. Pessino A; Sivori S; Bottino C; Malaspina A; Morelli L; Moretta L; Biassoni R; Moretta A, Molecular Cloning of NKp46: A Novel Member of the Immunoglobulin Superfamily Involved in Triggering of Natural Cytotoxicity. J. Exp. Med 1998, 188, 953–960. [PubMed: 9730896]

68. Wu J; Waxman DJ, Metronomic Cyclophosphamide Eradicates Large Implanted GL261 Gliomas by Activating Antitumor CD8(+) T-Cell Responses and Immune Memory. Oncoimmunology 2015, 4, e1005521–e1005521. [PubMed: 26137402]

69. Munn DH, Indoleamine 2,3-Dioxygenase, Tregs and Cancer. Curr. Med. Chem 2011, 18, 2240–6. [PubMed: 21517755]

70. Gomes B; Driessens G; Bartlett D; Cai D; Cauwenberghs S; Crosignani S; Dalvie D; Denies S; Dillon CP; Fantin VR; Guo J; Letellier M-C; Li W; Maegley K; Marillier R; Miller N; Pirson R; Rabolli V; Ray C; Streiner N; Torti VR; Tsaparikos K; Van den Eynde BJ; Wythes M; Yao L-C; Zheng X; Tumang J; Kraus M, Characterization of the Selective Indoleamine 2,3-Dioxygenase-1 (IDO1) Catalytic Inhibitor EOS200271/PF-06840003 Supports IDO1 as a Critical Resistance

Mechanism to PD-(L)1 Blockade Therapy. Mol. Cancer Ther 2018, 17, 2530–2542. [PubMed: 30232146]

71. Lechner MG; Karimi SS; Barry-Holson K; Angell TE; Murphy KA; Church CH; Ohlfest JR; Hu P; Epstein AL, Immunogenicity of Murine Solid Tumor Models as a Defining Feature of *in Vivo* Behavior and Response to Immunotherapy. J. Immunother 2013, 36, 477–489. [PubMed: 24145359]
72. Mei K-C Engineering Triggerable Liposome-Nanoparticle Hybrids as Novel Multifunctional Drug Delivery System. University College London (UCL School of Pharmacy), 2011.
73. Al-Ahmady Z; Lozano N; Mei K-C; Al-Jamal WT; Kostarelos K, Engineering Thermosensitive Liposome-Nanoparticle Hybrids Loaded With Doxorubicin for Heat-Triggered Drug Release. Int. J. Pharm 2016, 514, 133–141. [PubMed: 27863656]
74. Polverini PJ; Novak RF, Inhibition of Angiogenesis by The Antineoplastic Agents Mitoxantrone and Bisantrene. Biochem. Biophys. Res. Commun 1986, 140, 901–907. [PubMed: 2430572]
75. Steiner R, Angiostatic Activity of Anticancer Agents in The Chick Embryo Chorioallantoic Membrane (CHE-CAM) Assay. In Angiogenesis: Key Principles — Science — Technology — Medicine, Steiner R; Weisz PB; Langer R, Eds. Birkhäuser Basel: Basel, 1992; pp 449–454.
76. Iigo M; Shimamura M; Sagawa K; Tsuda H, Characteristics of the Inhibitory Effect of Mitoxantrone and Pirarubicin on Lung Metastases of Colon Carcinoma 26. Jpn. J. Cancer Res 1995, 86, 867–872. [PubMed: 7591965]
77. Ferrari L; Fichera A, Neoadjuvant Chemoradiation Therapy and Pathological Complete Response in Rectal Cancer. Gastroenterol. Rep 2015, 3, 277–288.
78. Cohen LF; Breslin TM; Kuerer HM; Ross MI; Hunt KK; Sahin AA, Identification and Evaluation of Axillary Sentinel Lymph Nodes in Patients With Breast Carcinoma Treated With Neoadjuvant Chemotherapy. Am. J. Surg. Pathol 2000, 24, 1266–72. [PubMed: 10976701]
79. Dosset M; Vargas TR; Lagrange A; Boidot R; Végran F; Roussey A; Chalmin F; Dondaine L; Paul C; Lauret Marie-Joseph E; Martin F; Ryffel B; Borg C; Adotevi O; Ghiringhelli F; Apetoh L, PD-1/PD-L1 Pathway: An Adaptive Immune Resistance Mechanism to Immunogenic Chemotherapy in Colorectal Cancer. Oncoimmunology 2018, 7, e1433981. [PubMed: 29872568]
80. Rosenberg JE; Hoffman-Censits J; Powles T; van der Heijden MS; Balar AV; Necchi A; Dawson N; O'Donnell PH; Balmanoukian A; Loriot Y; Srinivas S; Retz MM; Grivas P; Joseph RW; Galsky MD; Fleming MT; Petrylak DP; Perez-Gracia JL; Burris HA; Castellano D; Canil C; Bellmunt J; Bajorin D; Nickles D; Bourgon R; Frampton GM; Cui N; Mariathasan S; Abidoye O; Fine GD; Dreicer R, Atezolizumab in Patients with Locally Advanced and Metastatic Urothelial Carcinoma Who Have Progressed Following Treatment With Platinum-Based Chemotherapy: A Single-Arm, Multicentre, Phase 2 Trial. Lancet 2016, 387, 1909–20. [PubMed: 26952546]
81. Prendergast GC; Malachowski WP; DuHadaway JB; Muller AJ, Discovery of IDO1 Inhibitors: From Bench to Bedside. Cancer Research 2017, 77, 6795–6811. [PubMed: 29247038]
82. Wu Q; Jiang L; Li S.-c.; He Q.-j.; Yang B; Cao J, Small Molecule Inhibitors Targeting The PD-1/PD-L1 Signaling Pathway. Acta Pharmacol. Sin 2020.
83. Kopalli SR; Kang TB; Lee KH; Koppula S, Novel Small Molecule Inhibitors of Programmed Cell Death (PD)-1, and its Ligand, PD-L1 in Cancer Immunotherapy: A Review Update of Patent Literature. Recent. Pat. Anticancer Drug Discov 2019, 14, 100–112. [PubMed: 30370857]
84. van der Zanden SY; Luimstra JJ; Neefjes J; Borst J; Ovaa H, Opportunities for Small Molecules in Cancer Immunotherapy. Trends Immunol. 2020, 41, 493–511. [PubMed: 32381382]
85. Chen S; Song Z; Zhang A, Small-Molecule Immuno-Oncology Therapy: Advances, Challenges and New Directions. Curr. Top. Med. Chem 2019, 19, 180–185. [PubMed: 30854972]
86. Braunstein MJ; Kucharczyk J; Adams S, Targeting Toll-Like Receptors for Cancer Therapy. Target. Oncol 2018, 13, 583–598. [PubMed: 30229471]
87. Rosenblum D; Joshi N; Tao W; Karp JM; Peer D, Progress and Challenges Towards Targeted Delivery of Cancer Therapeutics. Nat. Commun 2018, 9, 1410. [PubMed: 29650952]
88. Tannock IF; Osoba D; Stockler MR; Ernst DS; Neville AJ; Moore MJ; Armitage GR; Wilson JJ; Venner PM; Coppin CM; Murphy KC, Chemotherapy with Mitoxantrone Plus Prednisone or Prednisone Alone for Symptomatic Hormone-Resistant Prostate Cancer: a Canadian Randomized Trial with Palliative End Points. J. Clin. Oncol 1996, 14 (6), 1756–64. [PubMed: 8656243]

89. Heidemann E; Stoeger H; Souchon R; Hirschmann WD; Bodenstein H; Oberhoff C; Fischer JT; Schulze M; Clemens M; Andreesen R; Mahlke M; König M; Scharl A; Fehnle K; Kaufmann M, Is First-Line Single-Agent Mitoxantrone in The Treatment of High-Risk Metastatic Breast Cancer Patients as Effective as Combination Chemotherapy? No Difference in Survival but Higher Quality of Life Were Found in a Multicenter Randomized Trial. Ann. Oncol 2002, 13, 1717–1729. [PubMed: 12419743]

90. Armitage JO, The Role of Mitoxantrone in Non-Hodgkin's Lymphoma. Oncology 2002, 16, 490–502, 507-8; discussion 511-2, 514. [PubMed: 12017536]

91. Wu C-C; Li Y-C; Wang Y-R; Li T-K; Chan N-L, On The Structural Basis and Design Guidelines For Type II Topoisomerase-Targeting Anticancer Drugs. Nucleic Acids Res. 2013, 41, 10630–10640. [PubMed: 24038465]

92. Mazerski J; Martelli S; Borowski E, The Geometry of Intercalation Complex of Antitumor Mitoxantrone and Ametantrone with DNA: Molecular Dynamics Simulations. Acta Biochim. Pol 1998, 45, 1–11. [PubMed: 9701490]

93. Kapuscinski J; Darzynkiewicz Z, Interactions of Antitumor Agents Ametantrone and Mitoxantrone (Novatrone) with Double-Stranded DNA. Biochem. Pharmacol 1985, 34, 4203–13. [PubMed: 4074383]

94. Scott LJ; Figgitt DP, Mitoxantrone: A Review of Its Use in Multiple Sclerosis. CNS Drugs 2004, 18, 379–96. [PubMed: 15089110]

95. Acebes-Huerta A; Lorenzo-Herrero S; Folgueras AR; Huergo-Zapico L; Lopez-Larrea C; Lopez-Soto A; Gonzalez S, Drug-Induced Hyperploidy Stimulates an Antitumor NK Cell Response Mediated by NKG2D and DNAM-1 Receptors. Oncoimmunology 2015, 5, e1074378–e1074378. [PubMed: 27057443]

96. Di Modica M; Sfondrini L; Regondi V; Varchetta S; Oliviero B; Mariani G; Bianchi GV; Generali D; Balsari A; Triulzi T; Tagliabue E, Taxanes Enhance Trastuzumab-Mediated ADCC on Tumor Cells Through NKG2D-mediated NK Cell Recognition. Oncotarget 2016, 7, 255–265. [PubMed: 26595802]

97. Truxova I; Kasikova L; Salek C; Hensler M; Lysak D; Holicek P; Bilkova P; Holubova M; Chen X; Mikyskova R; Reinis M; Kovar M; Tomalova B; Kline JP; Galluzzi L; Spisek R; Fucikova J, Calreticulin Exposure on Malignant Blasts Correlates With Improved Natural Killer Cell-Mediated Cytotoxicity in Acute Myeloid Leukemia Patients. Haematologica 2019, 105, 1868–1878. [PubMed: 31582537]

98. Fucikova J; Kline JP; Galluzzi L; Spisek R, Calreticulin Arms NK Cells Against Leukemia. Oncoimmunology 2019, 9, 1671763–1671763. [PubMed: 32002282]

99. Lan Y; Liang Q; Sun Y; Cao A; Liu L; Yu S; Zhou L; Liu J; Zhu R; Liu Y, Codelivered Chemotherapeutic Doxorubicin via a Dual-Functional Immunostimulatory Polymeric Prodrug for Breast Cancer Immunochemotherapy. ACS Appl. Mater. Interfaces 2020, 12, 31904–31921. [PubMed: 32551517]

100. Gao F; Zhang C; Qiu W-X; Dong X; Zheng D-W; Wu W; Zhang X-Z, PD-1 Blockade for Improving the Antitumor Efficiency of Polymer–Doxorubicin Nanoprodrug. Small 2018, 14, 1802403.

101. Greco FA; Coletti A; Custodi C; Dolciami D; Michele AD; Carotti A; Marinozzi M; Schlinck N; Macchiarulo A, Binding Properties of Different Categories of IDO1 Inhibitors: A Microscale Thermophoresis Study. Future Med. Chem 2017, 9, 1327–1338. [PubMed: 28771024]

102. Günther J; Däbritz J; Wirthgen E, Limitations and Off-Target Effects of Tryptophan-Related IDO Inhibitors in Cancer Treatment. Front. Immunol 2019, 10, 1801. [PubMed: 31417567]

103. Berrong Z; Mkrtichyan M; Ahmad S; Webb M; Mohamed E; Okoev G; Matevosyan A; Shrimali R; Eid RA; Hammond S; Janik JE; Khleif SN, Antigen-Specific Antitumor Responses Induced by OX40 Agonist Are Enhanced by the IDO Inhibitor Indoximod. Cancer Immunol. Res 2018, 6, 201–208. [PubMed: 29305519]

104. Zakharia Y; Rixe O; Ward JH; Drabick JJ; Shaheen MF; Milhem MM; Munn D; Kennedy EP; Vahanian NN; Link CJ; McWilliams RR, Phase 2 Trial of the IDO Pathway Inhibitor Indoximod Plus Checkpoint Inhibition for The Treatment of Patients With Advanced Melanoma. J. Clin. Oncol 2018, 36, 9512–9512.

105. Kumar S; Jaipuri FA; Waldo JP; Potturi H; Marcinowicz A; Adams J; Van Allen C; Zhuang H; Vahanian N; Link C; Brincks EL; Mautino MR, Discovery of Indoximod Prodrugs and Characterization of Clinical Candidate NLG802. Eur. J. Med. Chem 2020, 198, 112373. [PubMed: 32422549]

106. Yu JW; Bhattacharya S; Yanamandra N; Kilian D; Shi H; Yadavilli S; Katlinskaya Y; Kaczynski H; Conner M; Benson W; Hahn A; Seestaller-Wehr L; Bi M; Vitali NJ; Tsvetkov L; Halsey W; Hughes A; Traini C; Zhou H; Jing J; Lee T; Figueroa DJ; Brett S; Hopson CB; Smothers JF; Hoos A; Srinivasan R, Tumor-Immune Profiling of Murine Syngeneic Tumor Models as A Framework to Guide Mechanistic Studies and Predict Therapy Response in Distinct Tumor Microenvironments. PLoS One 2018, 13, e0206223–e0206223. [PubMed: 30388137]

107. Chen Daniel S.; Mellman I, Oncology Meets Immunology: The Cancer-Immunity Cycle. Immunity 2013, 39, 1–10. [PubMed: 23890059]

108. Jiménez-Sánchez A; Cybulska P; Mager KL; Koplev S; Cast O; Couturier D-L; Memon D; Selenica P; Nikolovski I; Mazaheri Y; Bykov Y; Geyer FC; Macintyre G; Gavarró LM; Drews RM; Gill MB; Papanastasiou AD; Sosa RE; Soslow RA; Walther T; Shen R; Chi DS; Park KJ; Hollmann T; Reis-Filho JS; Markowetz F; Beltrao P; Vargas HA; Zamarin D; Brenton JD; Snyder A; Weigelt B; Sala E; Miller ML, Unraveling Tumor–Immune Heterogeneity in Advanced Ovarian Cancer Uncovers Immunogenic Effect of Chemotherapy. Nature Genetics 2020, 52, 582–593. [PubMed: 32483290]

109. Madore J; Vilain RE; Menzies AM; Kakavand H; Wilmott JS; Hyman J; Yearley JH; Kefford RF; Thompson JF; Long GV; Hersey P; Scolyer RA, PD-L1 Expression in Melanoma Shows Marked Heterogeneity Within And Between Patients: Implications for Anti-PD-1/PD-L1 Clinical Trials. Pigm. Cell Melanoma Res 2015, 28, 245–253.

110. Suda K; Murakami I; Yu H; Kim J; Ellison K; Rivard CJ; Mitsudomi T; Hirsch FR, Heterogeneity in Immune Marker Expression after Acquisition of Resistance to EGFR Kinase Inhibitors: Analysis of A Case Wth Small Cell Lung Cancer Transformation. J. Thorac. Oncol 2017, 12, 1015–1020. [PubMed: 28193529]

111. Schalper KA; Carvajal-Hausdorf D; McLaughlin J; Altan M; Velcheti V; Gaule P; Sanmamed MF; Chen L; Herbst RS; Rimm DL, Differential Expression and Significance of PD-L1, IDO-1, and B7-H4 in Human Lung Cancer. Clin. Cancer Res 2017, 23, 370–378. [PubMed: 27440266]

112. Gide TN; Allanson BM; Menzies AM; Ferguson PM; Madore J; Saw RPM; Thompson JF; Long GV; Wilmott JS; Scolyer RA, Inter- And Intrapatient Heterogeneity of Indoleamine 2,3-Dioxygenase Expression in Primary and Metastatic Melanoma Cells and The Tumour Microenvironment. Histopathology 2019, 74, 817–828. [PubMed: 30589949]

113. Lorusso D; Di Stefano A; Carone V; Fagotti A; Pisconti S; Scambia G, Pegylated Liposomal Doxorubicin-Related Palmar-Plantar Erythrodysesthesia (‘Hand-Foot’ Syndrome). Ann. Oncol 2007, 18, 1159–1164. [PubMed: 17229768]

114. Stewart JCM, Colorimetric Determination of Phospholipids With Ammonium Ferrothiocyanate. Anal. Biochem 1980, 104 (1), 10–14. [PubMed: 6892980]

115. Faustino-Rocha A; Oliveira PA; Pinho-Oliveira J; Teixeira-Guedes C; Soares-Maia R; da Costa RG; Colaço B; Pires MJ; Colaço J; Ferreira R; Ginja M, Estimation of Rat Mammary Tumor Volume Using Caliper and Ultrasonography Measurements. Lab Animal 2013, 42, 217–24. [PubMed: 23689461]

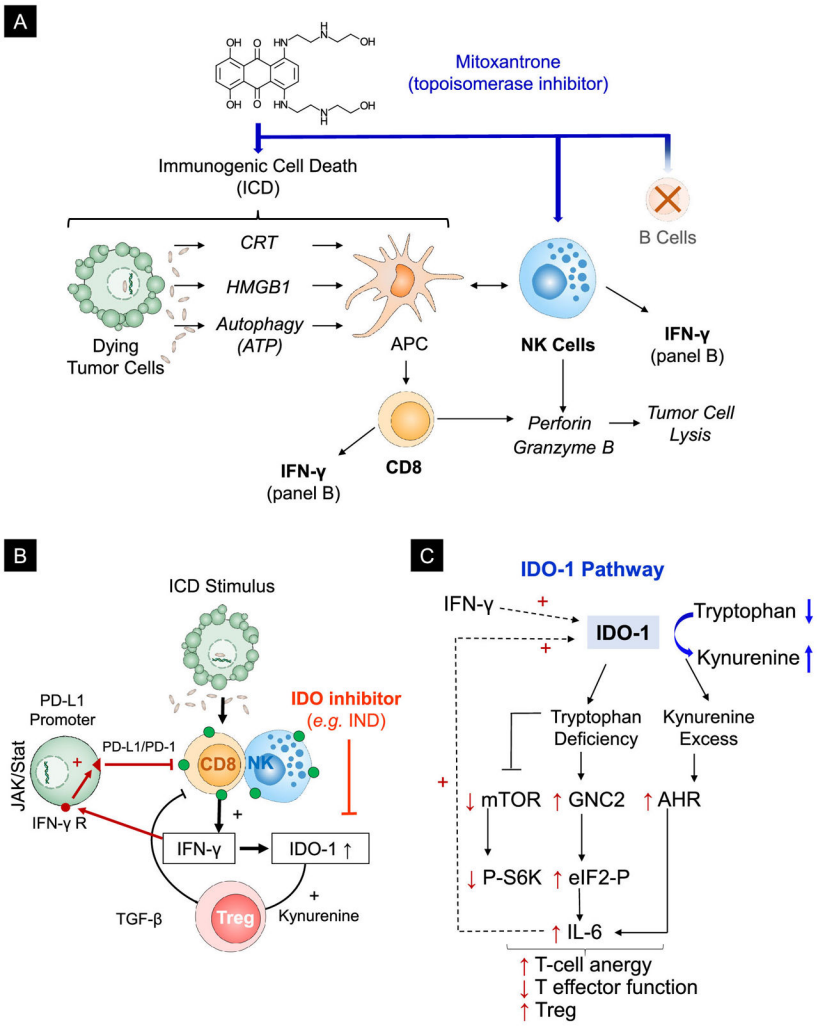

Figure 1. The rationale for the combined use of an ICD inducer and an IDO-1 inhibitor.

(A) Schematic illustration of the processes involved in MTO-induced immunogenic cell death (ICD). ICD facilitates tumor antigen cross-presentation by APC cells by promoting a cell death response that is accompanied by CRT expression on the dying tumor cell surface. CRT provides an “eat-me” signal for APC uptake. In addition, the release of adjuvant stimuli from the dying tumor cells, *e.g.,* HMGB1 from the nucleus and ATP from autophagic vesicles, are responsible for DC maturation and antigen presentation to cognate immune cells. The immunogenic effects of MTO include the recruitment of NK cells and $CD8^{low}$ CTL, which are capable of inducing tumor cell lysis by releasing granzyme B and perforin. [13] Both cell types also produce IFN-γ. (B) Mechanistic explanation of the counter-regulatory effect of IFN-γ release on the ICD response by upregulating IDO-1 and PD-L1 expression, as well as Treg generation. (C) Schematic illustration of the role of IDO-1 in regulating the tumor microenvironment. IDO-1 exerts an immune suppressive effect by converting tryptophan to kynurenine. The kynurenine excess and tryptophan depletion leads to interference in the mTOR pathway and P-S6 kinase activity but enhances the activation of a kinase known as “general control nonderepressible 2” (GNC2) as well as the transcriptional activity of the aryl hydrocarbon receptor (AhR). This results in decreased

cytotoxic T cell activity, T-cell anergy, and increased Treg production. In addition, the activation of increased IL-6 production by the AhR is responsible for more IDO-1 production.

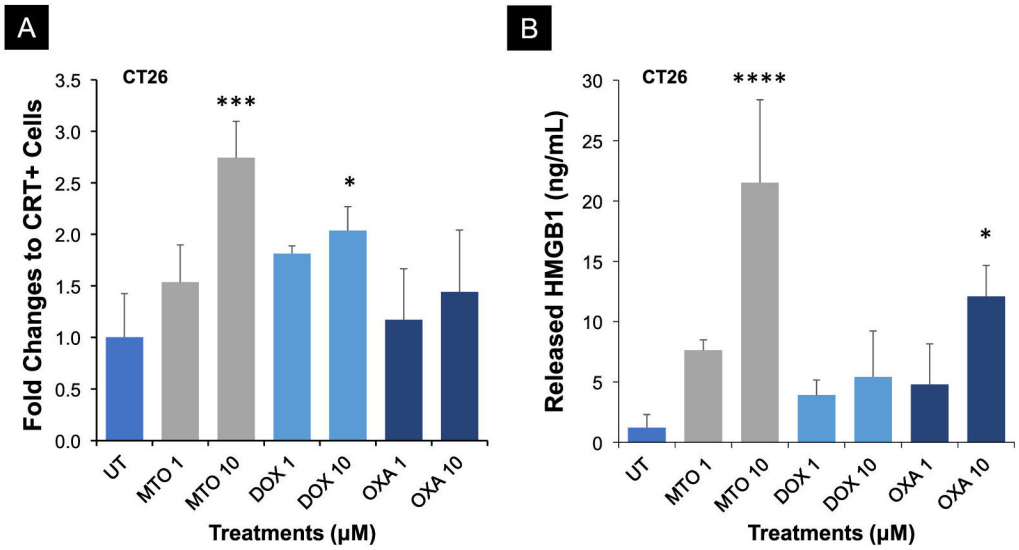

Figure 2. MTO generates a strong ICD response in CT26 colon cancer cells.

(A) CRT surface detection by flow cytometry. CT26.WT cells were treated by MTO, DOX, and OXA at 1 and 10 μM for 24 h. (B) *In Vitro* measurement of extracellular HMGB1 release by CT26.WT cells after exposure to MTO, DOX, and OXA treatments for 24h. HMGB1 levels were determined in the cellular supernatants by an ELISA kit. Data are presented as fold-change (mean ± S.D., $n = 3$) when compared to the untreated group (ANOVA, post hoc = Fisher's, *$p < 0.05$, ***$p < 0.001$, ****$p < 0.0001$).

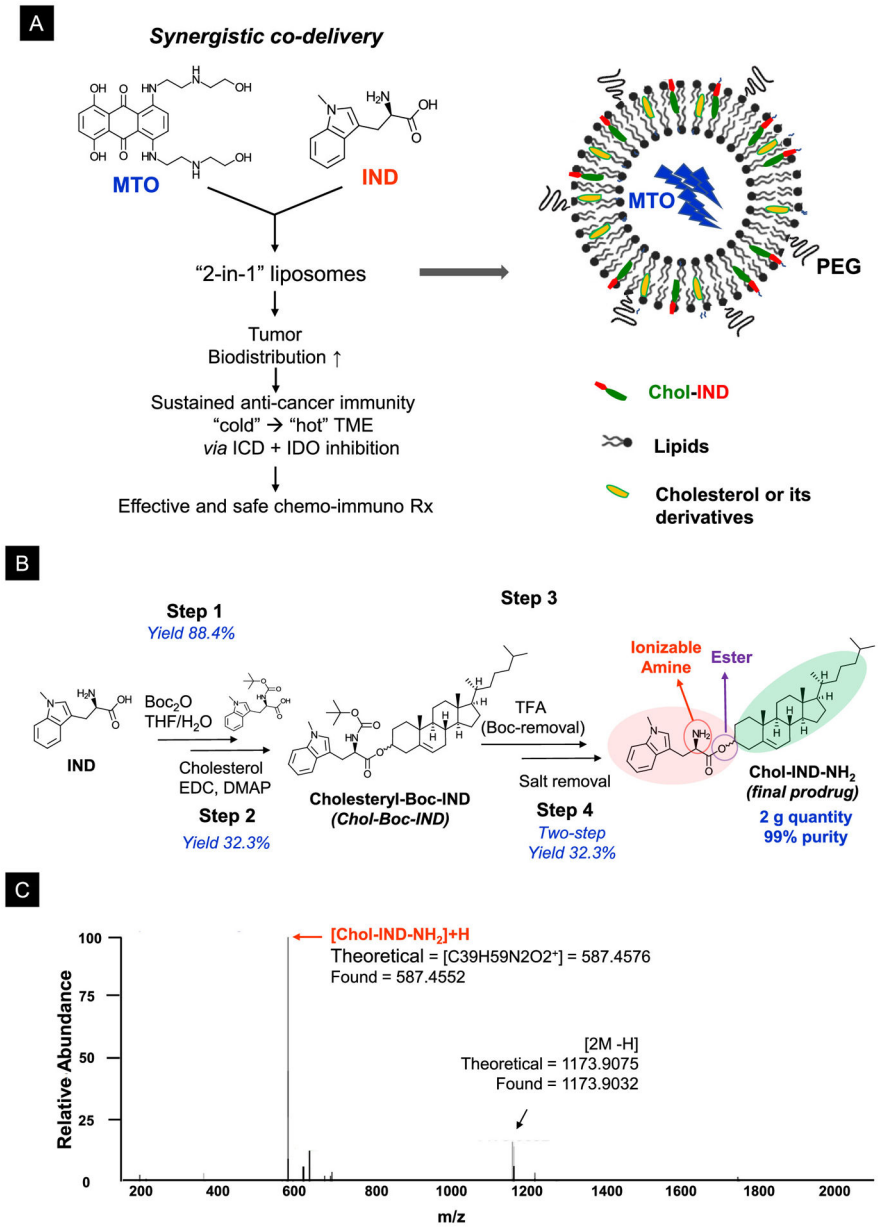

Figure 3. Synthesis of the IND prodrug for liposome construction.

(A) Schematic illustration to show the envisaged combination of MTO and IND as a "2-in-1" liposome that delivers a strong ICD stimulus, contemporaneous with the interference of the counter-regulatory effect of IDO-1 in the TME. The dual-delivery liposome is synthesized by embedding the IND prodrug into the lipid bilayer of the liposome, which can also be remote-loaded with MTO. Remote pleading leads to the crystallization of the protonated drug in the liposomal interior. (B) Schematic to depict the 4-step process for the synthesis of the Chol-IND prodrug, including the use of conjugation chemistry for the ester linkage of IND to cholesterol. (C) High-resolution spectra from mass spectroscopy confirm the synthesis of the Chol-IND prodrug. More detailed information about the characterization

of the reaction intermediates and the final product by ^{1}H NMR and HR-MS is described in Figure S1.

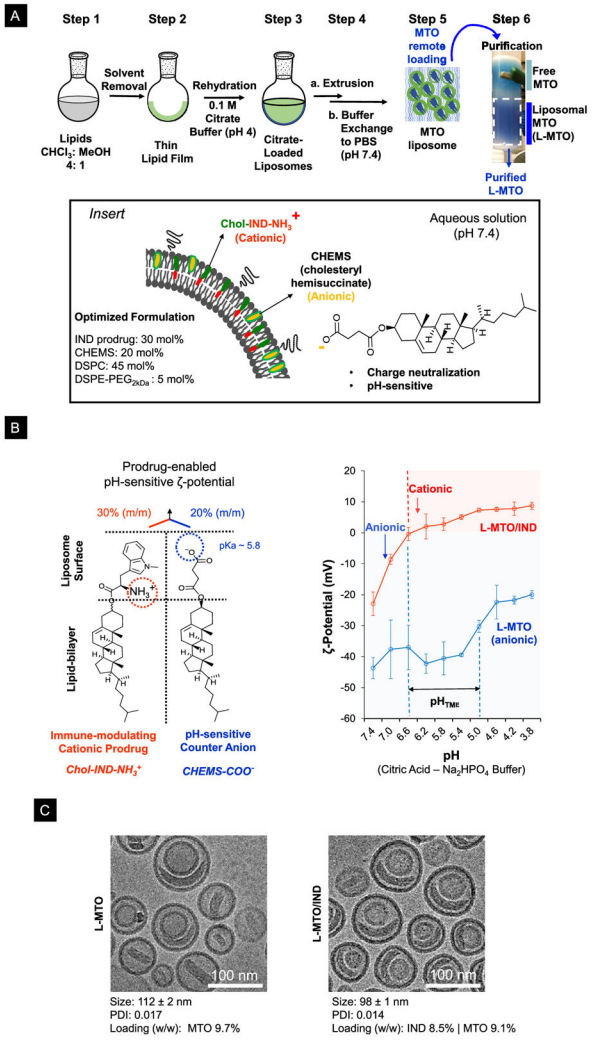

Figure 4. Synthesis of the MTO/IND dual-delivery liposome.

(A) Schematic to outline the liposome synthesis steps. Briefly, DSPC, Chol-IND, cholesteryl hemisuccinate (CHEMS), and DSPE-PEG_{2kDa} at a molar ratio of 45: 30: 20: 5, was dissolved in $CHCl_3$ (step 1), prior to solvent evaporation to form a lipid film (step 2). The lipid film was hydrated in a citric acid-sodium citrate buffer solution at pH 4 (step 3), followed by membrane extrusion, and elution over a desalting column to remove citric acid (step 4). MTO was remotely loaded into the liposomes by generating a citrate gradient (step 5). The non-encapsulated MTO was removed over a Sephadex G-25 column to obtain the purified MTO liposome (L-MTO) in step 6. Insert box: Use of CHEMS to neutralize the positive charge of the IND prodrug. The rationale for this procedure is described in more detail in Figure S2. (B) Schematic to illustrate the impact of the prodrug and CHEMS on the ζ-potential. The Chol-IND-NH_3^+ prodrug introduces a cationic charge, while CHEMS-COO^- introduces an anionic charge. To demonstrate the effect of pH on the ζ-potential of the L-MTO/IND and L-MTO liposomes, the carriers exchanged into a citric acid sodium phosphate (Na_2HPO_4) buffer system in which the pH was lowered by incrementally increasing the amount of citric acid. This demonstrated that the change in pH change was

accompanied by a continuous shift in the carrier ζ-potential, which differed between the liposome species. Thus, while the ζ-potential for L-MTO/IND changed from −23 ± 4 mV at pH 7.4 to 9 ± 1 mV at pH 3.8, the L-MTO liposomes maintained an anionic charge throughout. (C) CryoEM macrograph to show the morphological similarity between L-MTO and L-MTO/IND liposomes, including the presence of the trapped MTO drug precipitate. The panel also shows the data for the hydrodynamic size, polydispersity index (PDI), and drug loading levels (drug/lipid w/w%) of the liposomes.

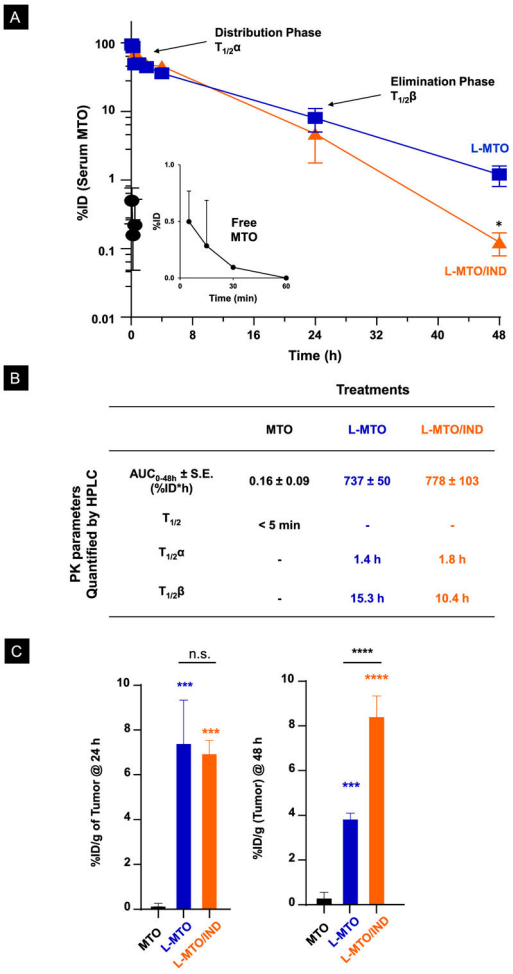

Figure 5. Pharmacokinetics and tumor uptake of free and liposomal MTO.

(A) CT26 tumor-bearing Balb/c mice were used for the PK study, 14 days post-tumor inoculation. MTO, L-MTO, L-MTO/IND were given in one IV bolus injection at an MTO-equivalent dose at 3 mg/kg. Blood was collected at 15 min, 30 min, 1 h, 2 h, 4 h, 24 h, and 48 h post-injection (n = 3/time point). The percentages of injected MTO dose (%ID) in serum measured by HPLC were shown. Both L-MTO and L-MTO/IND significantly increased serum drug concentration. (B) The pharmacokinetic parameters, *i.e.,* the area under the curve (AUC), distribution, and elimination half-time of the liposomes ($T_{1/2}\alpha$ and $T_{1/2}\beta$, respectively) are summarized in the table. (C) Tumor MTO concentrations at 24h and 28 h post-injection are shown. Data were normalized as %ID per gram of tissue (%ID/g). Both L-MTO and L-MTO/IND showed similar tumor biodistribution at 24 h. The L-MTO/IND showed better tumor retention at 48 h when compared to L-MTO. Data were expressed as mean ± SD, $n = 3$. (ANOFA, post hoc = Tukey's: *p<0.05; **$p < 0.01$, ***$p <$ 0.001, ****$p < 0.001$, n.s. $p > 0.05$).

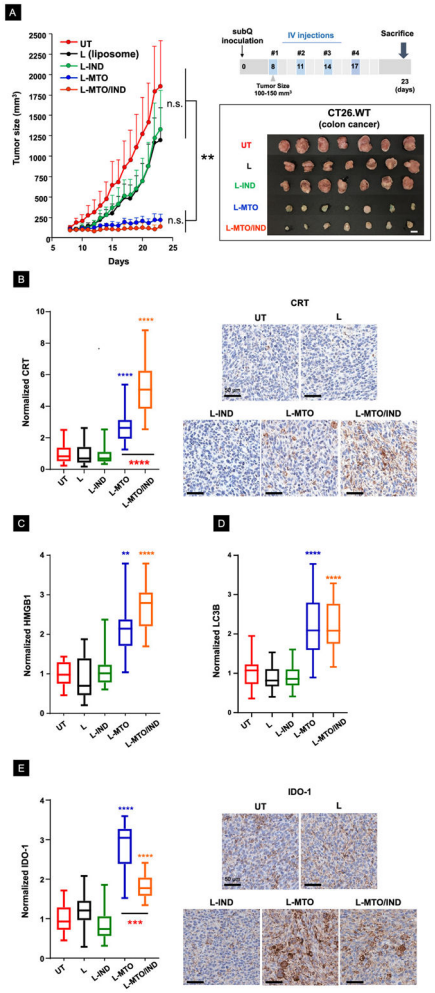

Figure 6. The liposomal MTO/IND combination provides effective interference in colon cancer growth through ICD induction and IDO-1 inhibition.

Experimental timeline for the efficacy study: a subcutaneous syngeneic colon cancer model was established by injecting CT26 cells into the right flank of Balb/c mice (day 0). After reaching tumor sizes of 100-150 mm^3, animals received IV injection of nanocarriers on 4 occasions (day 8, 11, 14, 17), as depicted in the schematic. Animals were sacrificed on day 23 to remove tumor tissue for the performance of immunophenotype analysis. The L-MTO/IND liposome was IV injected to deliver MTO and IND doses of 3 mg/kg and 2.8 mg/kg per injection, respectively. Treatment was compared to injection of saline (UT), MTO-only liposomes (L-MTO), L-IND (IND liposome without MTO), and L (empty liposomes without MTO and IND). (A). Live animal tumor growth curves (mean ± S.D., $n = 7$) plus photographs of harvested tumors on day 23. The inhibition of tumor growth by L-MTO and L-MTO/IND is significant compared to UT and other controls (** $p < 0.01$, ANOVA) but not significantly different between L-MTO and L-MTO/IND on day 23. (B) Quantification and representative IHC staining images for CRT confirmed ICD induction by L-MTO liposomes, which was further enhanced by the dual drug delivery. (C-D) IHC staining confirmed a significant induction of HMGB1 and LC3B upon L-MTO and L-MTO/IND treatment. (E) IHC staining revealed a significant induction of IDO-1 expression

upon L-MTO treatment. While L-MTO/IND also induced significant IDO-1 expression (when compared to the controls), co-delivery of IND reduced the level of the IDO-1 response when compared to L-MTO. (ANOVA, post hoc = Tukey's test: $^{**}p < 0.01$, $^{***}p < 0.001$, $^{****}p < 0.0001$).

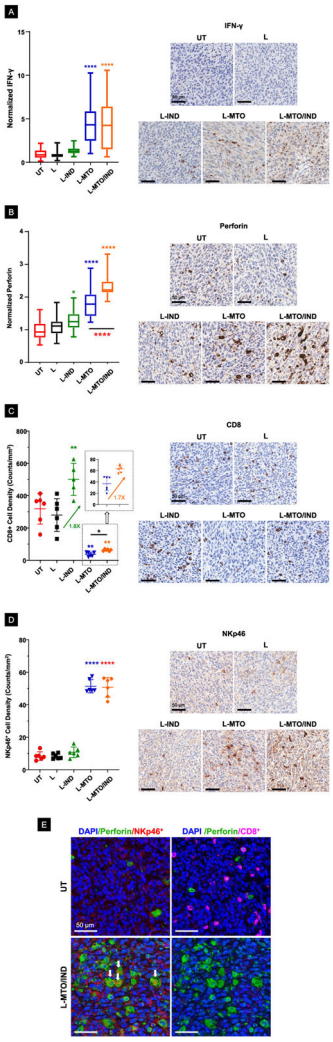

Figure 7. The dual delivery liposome also induced cognate immune responses in the efficacy study discussed in Figure 6.

(A-B) Quantification and representative IHC images for IFN-γ and perforin expression. Our data showed that L-MTO/IND liposome was able to trigger a more effective elevation of both markers at the tumor site when compared to L-MTO. (C-D) Quantification of $CD8^+$ $NKp46^+$ cells, along with representative IHC images. The data show a significant reduction of the $CD8^+$ cell number/mm^2, in parallel with an increased number of $NKp46^+$ cells in response to liposomal MTO delivery. (E) Multiplexing IHC showing the co-localization of DAPI-labeled nucleus (blue), FITC-labeled perforin (green), TRITC-labeled NKp46+ cells (red) and Opal-480-labeled CD8+ cells (magenta). The perforin$^+$CD8$^+$ and perforin $^+$NKp46$^+$ double-positive cells are labeled by white arrows. MTO significantly decreased perforin$^+$CD8$^+$ cells but increased perforin$^+$NKp46$^+$ cells. IND, on the other hand, increased perforin$^+$CD8$^+$ cell density significantly in the absence or presence of MTO (ANOVA post hoc = Tukey's test: *$p < 0.05$, **$p < 0.01$, ***$p < 0.001$, ****$p < 0.0001$).

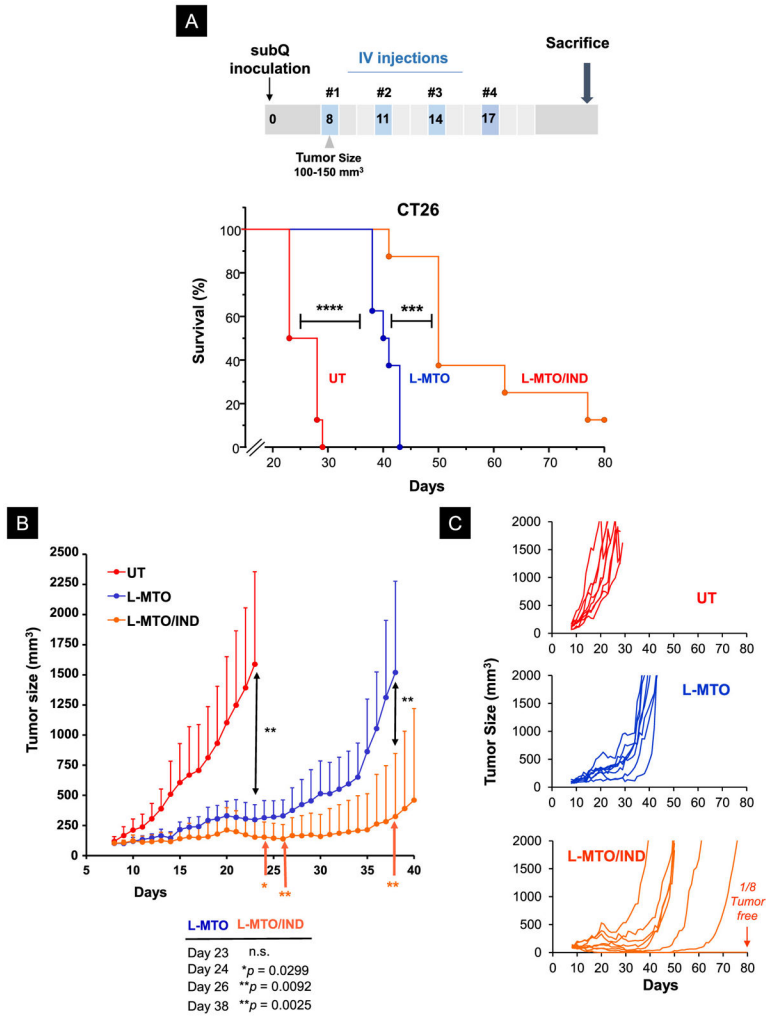

Figure 8. The dual-delivery liposome significantly improved survival outcome in the CT26 colon cancer model.

The experimental schedule is identical to the efficacy study in Figure 6, except that the animals were sacrificed when approach end-of-life criteria, as determined by the approved animal protocol. (A) Kaplan-Meier analysis to show that L-MTO significantly improved survival when compared to the untreated controls (Log-rank/Mantel-Cox test, $n = 8$, Chi-square 16.55, ****$p < 0.0001$). IND co-delivery with MTO leads to a highly significant increase in animal survival over L-MTO treatment, with 1 out of 8 mice ended up tumor-free. (Log-rank/Mantel-Cox test, $n = 8$, Chi-square 11.62, ***$p = 0.0007$) (B) Averaged tumor growth curves to show that L-MTO and L-MTO/IND were equally efficient at inhibiting tumor growth by day 23 compared to the untreated control (Brown-Forsythe ANOVA test F(2, 7.8) = 24.01, ***p= 0.005, post hoc = Dunnett's T3 test: **$p = 0.0063$ and 0.0035 for L-MTO *vs.* UT and L-MTO/IND *vs.* UT, respectively. L-MTO *versus* L-MTO/IND $p = 0.1081$ at day 23). However, from day 24 onwards, the co-delivery L-MTO/IND liposome was significantly more effective than L-MTO through the duration of the study. (unpaired t-test day 24 t(14) = 2.418, *$p = 0.0299$; day 25 t(14) = 2.726, *$p = 0.0164$; day 28 t(14) = 3.021, **$p = 0.0092$; day 38 t(14) = 3.675, **$p = 0.0025$) (C) The

corresponding spaghetti tumor growth curves confirm that the most significant tumor growth inhibition was obtained by L-MTO/IND co-delivery when compared to L-MTO and untreated controls.

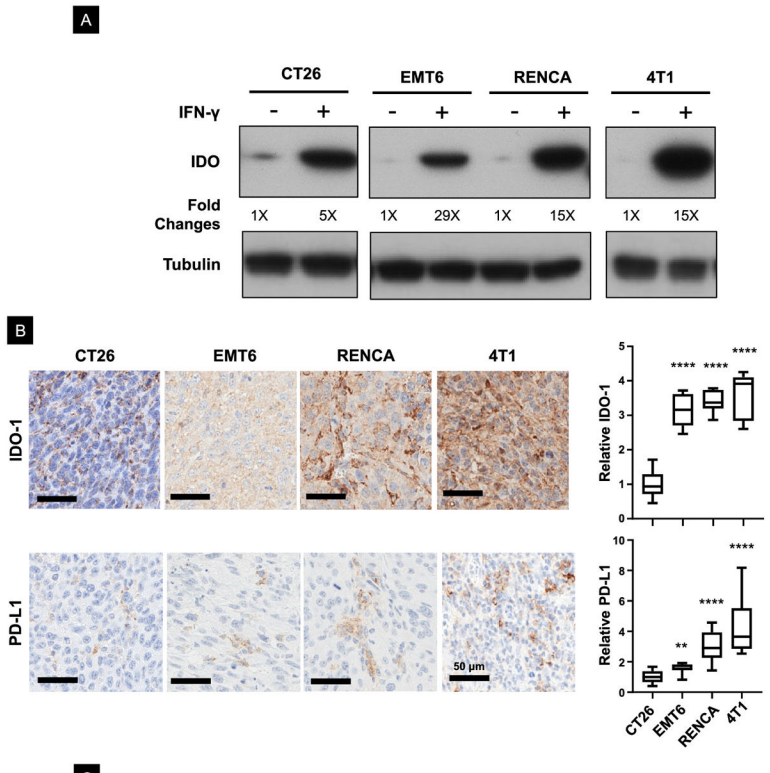

C

Stratification of Syngeneic Tumor Models

	CT26	EMT6	RENCA	4T1
IDO-1 expression (IFN-γ)*	+	+++	++	++
Cellular PD-L1 Expression†	+	+	+++	+
Basal Tumor IDO-1 Levels**	+	++	+++	+++
Basal Tumor PD-L1 Levels**	+	+	++	+++
ICI Responsiveness†	+++	++	++	-

* Cellular response to IFN-γ, Western Blotting (see Fig. 9B)
** Tumor characterized by quantitative IHC (See Fig. 9C)
† Characterization by Charles River Labs

Figure 9. Assessment of IDO-staining intensity in a range of cancer cells with distinct tumor microenvironments (TMEs).

(A) IDO-1 immunoblotting to compare the response of CT26 with other tumors in response to IFN-γ treatment. (B) IHC analysis of the basal IDO-1 and PD-L1 expression in 4 Balb/c syngeneic tumor models. EMT6, RENCA, and 4T1 models showed a significantly higher basal IDO-1 expression in their TMEs compared to CT26. We observed a lower level of PD-L1 expression in CT26, compared to EMT6, RENCA and 4T1 subcutaneous tumors. (C) Table summarizing the heterogeneous TME in 4 syngeneic tumor models based on immunological features such as PD-L1 and IDO-1 expression, as well as therapeutic responsiveness to ICIs. (ANOVA post hoc = Tukey's: $^{**}p < 0.01$, $^{****}p < 0.001$).

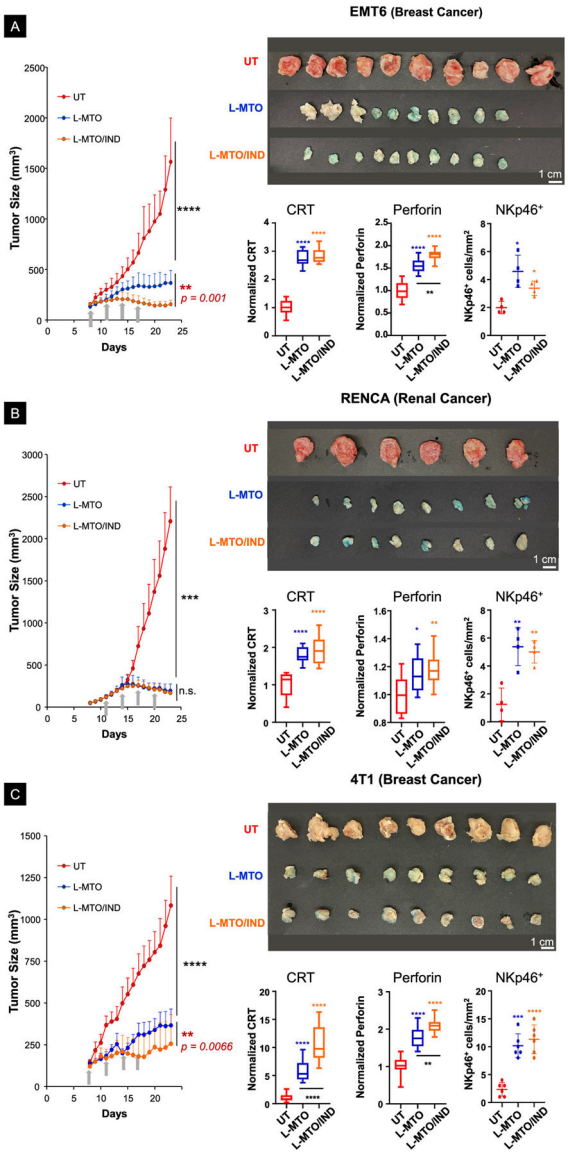

Figure 10. Liposomal combination therapy also provided effective tumor inhibition in EMT6, RENCA, and 4T1 tumor models.

(A-C) Live-animal tumor growth curves (mean ± SD, left-panel), photographs of tumors (upper-right panel), and the quantitative IHC analysis of CRT, perforin, and NKp46 (lower-right panel) from tumors harvested on day 23 in EMT6 (n = 10), RENCA (n = 6~8), and 4T1 (n = 9) cancer models, respectively. The co-delivery of IND by the dual delivery liposome significantly improved the tumor growth inhibition in both EMT6 and 4T1 breast cancer models, compared to L-MTO. It was difficult, however, to demonstrate an additive IND effect on the already-significant tumor inhibition by MTO in the war immune responsive RENCA cancer model. (ANOVA post hoc = Tukey's: n.s. $p > 0.05$, *$p < 0.05$, **$p < 0.01$, **** $p < 0.001$).